Energy Transport during 3D Small-scale Reconnection Driven by Anisotropic Plasma Turbulence

Jeffersson A. Agudelo Rueda[1,2] ⓘ, Daniel Verscharen[2] ⓘ, Robert T. Wicks[3] ⓘ, Christopher J. Owen[2] ⓘ, Georgios Nicolaou[2] ⓘ, Kai Germaschewski[4] ⓘ, Andrew P. Walsh[5] ⓘ, Ioannis Zouganelis[5] ⓘ, and Santiago Vargas Domínguez[6] ⓘ

[1] Department of Physics and Astronomy, Dartmouth College, Hanover, NH 03755, USA; jeffersson.a.agudelo.rueda@dartmouth.edu
[2] Mullard Space Science Laboratory, University College London, Holmbury St. Mary, Dorking, Surrey, RH5 6NT, UK
[3] Department of Mathematics, Physics and Electrical Engineering, Northumbria University, Newcastle upon Tyne, NE1 8ST, UK
[4] Space Science Center, University of New Hampshire, Durham, NH 03824, USA
[5] European Space Astronomy Centre, Urb. Villafranca del Castillo, E-28692 Villanueva de la Cañada, Madrid, Spain
[6] Universidad Nacional de Colombia, Observatorio Astronómico Nacional, Ed. 413 Bogotá, Colombia

Abstract

Energy dissipation in collisionless plasmas is a long-standing fundamental physics problem. Although it is well known that magnetic reconnection and turbulence are coupled and transport energy from system-size scales to subproton scales, the details of the energy distribution and energy dissipation channels remain poorly understood. Especially, the energy transfer and transport associated with 3D small-scale reconnection that occurs as a consequence of a turbulent cascade is unknown. We use an explicit fully kinetic particle-in-cell code to simulate 3D small-scale magnetic reconnection events forming in anisotropic and decaying Alfvénic turbulence. We identify a highly dynamic and asymmetric reconnection event that involves two reconnecting flux ropes. We use a two-fluid approach based on the Boltzmann equation to study the spatial energy transfer associated with the reconnection event and compare the power density terms in the two-fluid energy equations with standard energy-based damping, heating, and dissipation proxies. Our findings suggest that the electron bulk flow transports thermal energy density more efficiently than kinetic energy density. Moreover, in our turbulent reconnection event, the energy density transfer is dominated by plasma compression. This is consistent with turbulent current sheets and turbulent reconnection events, but not with laminar reconnection.

Unified Astronomy Thesaurus concepts: Solar magnetic reconnection (1504); Interplanetary turbulence (830)

1. Introduction

The solar wind in the inner heliosphere is a weakly collisional, turbulent plasma in which the energy is transported from large ($\sim 10^9$ km) to small ($\sim 10^{-1}$ km) scales via an active turbulent cascade (Coleman 1968; Marsch & Tu 1990). Although the collisionless nature of the solar wind precludes classical viscous dissipation of these turbulent fluctuations, the nonadiabatic evolution of the solar wind (Gazis & Lazarus 1982; Matteini et al. 2007; Hellinger et al. 2011) suggests the action of local heating mechanisms (Barnes 1968; Goldstein et al. 2015). The plasma physics processes responsible for this heating are not fully understood yet. The observed velocity distribution functions of the solar wind species often exhibit nonthermal features (e.g., Feldman et al. 1975, 1978; Marsch et al. 1982; McComas et al. 1992).

Important progress has been made to understand heating and energy dissipation (e.g., Gary 1999; Howes et al. 2017; Klein et al. 2017; Matthaeus et al. 2020). Landau damping, ion cyclotron damping, and stochastic heating are considered collisionless dissipation mechanisms that transfer energy from the electromagnetic field to the plasma particles (Marsch et al. 2003; Kasper et al. 2008; Chandran et al. 2010, 2013). The dissipation occurs predominantly in intermittent structures that form in plasma turbulence (Matthaeus et al. 1999; Kiyani et al. 2015).

Like turbulence, magnetic reconnection is a process that emerges on a broad range of scales and under a large variety of plasma conditions. Magnetic reconnection occurs when magnetic structures form regions in which the frozen-in condition is locally broken, allowing the exchange of particles between the magnetic structures (Hesse & Schindler 1988; Schindler et al. 1988).

Magnetic reconnection and turbulence are closely linked. Magnetic reconnection self-consistently occurs as a consequence of the turbulent cascade (Servidio et al. 2010; Loureiro & Boldyrev 2020; Agudelo Rueda et al. 2021), and turbulence emerges in current sheets, exhaust flows, electron streamers, and shocks associated with reconnection events (Kowal et al. 2017; Pucci et al. 2017; Lapenta et al. 2020). During magnetic reconnection, plasma particles are heated and accelerated while the magnetic field topology changes (Pontin 2011; Zweibel & Yamada 2016; Lazarian et al. 2020).

The role of magnetic reconnection for the evolution of energy in collisionless plasmas is unclear. Although magnetic reconnection transports energy from large to small scales (Sundkvist et al. 2007; Franci et al. 2017; Loureiro & Boldyrev 2020), the details of the energy transport across scales and the role of reconnection in the turbulent cascade are a matter of ongoing research (Franci et al. 2017; Loureiro & Boldyrev 2017; Adhikari et al. 2021). The energy transfer between fields and particles, and the transfer between kinetic and thermal degrees of freedom during reconnection are the key objectives of this research area.

The energy transfer and transport associated with magnetic reconnection have been addressed by previous studies that focus on idealized 2D Harris current sheet reconnection

(Yin et al. 2001; Schmitz & Grauer 2006; Wang et al. 2015; Pezzi et al. 2021), 3D laminar collisionless reconnection in the context of magnetospheres (Wang et al. 2018), and 2D reconnection in turbulent plasma (Fadanelli et al. 2021). In this work, we use particle-in-cell (PIC) simulations to study the energy transfer associated with 3D small-scale magnetic reconnection that self-consistently occurs as a consequence of an anisotropic turbulent cascade. In Section 2, we present our theoretical framework to study the energy transfer and transport in our plasma simulations. In Section 3, we present our simulation results, emphasizing the presence of agyrotropy in Section 3.3 and the energy distribution in Section 3.4. In Section 4, we discuss the implications of our results. In Section 5, we provide our conclusions.

2. Energy Transfer and Transport

The total energy in a closed volume of plasma is partitioned among the particles and the electromagnetic fields. The bulk kinetic energy density of the particle species s is associated with the first velocity moment of the particle velocity distribution function $f_s = f_s(\boldsymbol{x}, \boldsymbol{v}, t)$ and therefore with the bulk flux of the particles. The thermal energy density is associated with the second velocity moment and thus the pressure of the particles. The evolution of f_s follows the Boltzmann equation

$$\frac{\partial f_s}{\partial t} + \boldsymbol{v} \cdot \nabla f_s + \frac{q_s}{m_s}(\boldsymbol{E} + \boldsymbol{v} \times \boldsymbol{B}) \cdot \nabla_v f_s = \left(\frac{\partial f_s}{\partial t}\right)_c, \quad (1)$$

where $\boldsymbol{v}$ is the velocity, $\boldsymbol{E}$ is the electric field, $\boldsymbol{B}$ is the magnetic field, q_s is the charge of a particle, and m_s is the mass of a particle. The term $(\partial f_s/\partial t)_c$ on the right-hand side represents the change in the distribution function due to collisions. This term includes individual correlations between fields and particles, based on the particles' individual Coulomb potentials (Klimontovich 1997). To study the energy transport, we derive a set of energy equations based on the Boltzmann Equation (1). We first define the density

$$n_s \equiv \int f_s \, d^3v, \quad (2)$$

the bulk velocity

$$\boldsymbol{u}_s \equiv \frac{1}{n_s} \int f_s \boldsymbol{v} \, d^3v, \quad (3)$$

and the pressure tensor

$$\overline{\overline{\boldsymbol{P}}}_s \equiv m_s \int f_s (\boldsymbol{v} - \boldsymbol{u}_s)(\boldsymbol{v} - \boldsymbol{u}_s) \, d^3v, \quad (4)$$

where $(\boldsymbol{v} - \boldsymbol{u}_s)(\boldsymbol{v} - \boldsymbol{u}_s)$ is the dyadic product. We define the heat flux vector

$$\boldsymbol{h}_s \equiv \frac{1}{2} m_s \int f_s (\boldsymbol{v} - \boldsymbol{u}_s) \cdot (\boldsymbol{v} - \boldsymbol{u}_s)(\boldsymbol{v} - \boldsymbol{u}_s) \, d^3v. \quad (5)$$

We define the first moment of the collision term in Equation (1) as

$$\boldsymbol{\Xi}^1 = \int \boldsymbol{v} \left(\frac{\partial f_s}{\partial t}\right)_c d^3v \quad (6)$$

and the second moment as

$$\overline{\overline{\boldsymbol{\Xi}}}^2 = \int \boldsymbol{v}\boldsymbol{v} \left(\frac{\partial f_s}{\partial t}\right)_c d^3v. \quad (7)$$

With these definitions, we compute the first and second moments of Equation (1) (see the Appendix for details). The first moment of Equation (1) yields the kinetic energy equation

$$\frac{d\varepsilon_s^k}{dt} + \boldsymbol{u}_s \cdot \nabla \cdot \overline{\overline{\boldsymbol{P}}}_s + \varepsilon_s^k \nabla \cdot \boldsymbol{u}_s - q_s n_s(\boldsymbol{u}_s \cdot \boldsymbol{E}) = \Xi_s^k, \quad (8)$$

where $d/dt = \partial/\partial t + (\boldsymbol{u}_s \cdot \nabla)$ is the total time derivative,

$$\varepsilon_s^k = \frac{1}{2} n_s m_s(\boldsymbol{u}_s \cdot \boldsymbol{u}_s) \quad (9)$$

is the kinetic energy density, and

$$\Xi_s^k = m_s \boldsymbol{u}_s \cdot \boldsymbol{\Xi}_s^1 \quad (10)$$

represents the irreversible kinetic energy transfer. The terms $\boldsymbol{u}_s \cdot \nabla \cdot \overline{\overline{\boldsymbol{P}}}_s$, $\varepsilon_s^k \nabla \cdot \boldsymbol{u}_s$, and the advective term $(\boldsymbol{u}_s \cdot \nabla)\varepsilon_s^k$ are associated with the term $\boldsymbol{v} \cdot \nabla f_s$ in Equation (1). Therefore, these terms represent kinetic energy density transport due to the free streaming of particles. Conversely, the term $-q_s n_s(\boldsymbol{u}_s \cdot \boldsymbol{E})$, associated with the electric field, represents the energy density transfer between particle bulk flows and fields.

The second moment of Equation (1) yields the thermal energy equation

$$\frac{d\varepsilon_s^{\text{th}}}{dt} + \nabla \cdot \boldsymbol{h}_s + \nabla \boldsymbol{u}_s : \overline{\overline{\boldsymbol{P}}}_s + \varepsilon_s^{\text{th}} \nabla \cdot \boldsymbol{u}_s = \Xi_s^{\text{th}}, \quad (11)$$

where

$$\varepsilon_s^{\text{th}} = \frac{1}{2} \text{Tr}(\overline{\overline{\boldsymbol{P}}}_s) \quad (12)$$

is the thermal energy density and

$$\Xi_s^{\text{th}} = -m_s \boldsymbol{u}_s \cdot \boldsymbol{\Xi}^1 + \frac{m_s}{2} \text{Tr}(\overline{\overline{\boldsymbol{\Xi}}}^2) \quad (13)$$

represents the irreversible thermal energy transfer. The expression Tr stands for the trace of a tensor, and $\nabla \boldsymbol{u}_s : \overline{\overline{\boldsymbol{P}}}_s$ is the double contraction of the strain tensor $\nabla \boldsymbol{u}_s$ and $\overline{\overline{\boldsymbol{P}}}_s$. The terms $\nabla \cdot \boldsymbol{h}_s$, $\nabla \boldsymbol{u}_s : \overline{\overline{\boldsymbol{P}}}_s$, and $\varepsilon_s^{\text{th}} \nabla \cdot \boldsymbol{u}_s$, associated with $\boldsymbol{v} \cdot \nabla f_s$ in Equation (1), represent thermal energy density transport due to the free streaming of particles.

The terms on the left-hand sides of Equations (8) and (11) describe collisionless processes, whereas the terms on the right-hand sides describe collisional processes in the plasma that generate an increase in the plasma entropy.

Equations (8) and (11) alone do not capture total energy conservation because they do not account for the rate of change in the electromagnetic energy density $\partial \varepsilon^{\text{em}}/\partial t$, nor for the electromagnetic energy flux $\nabla \cdot \boldsymbol{S}$, where

$$\varepsilon^{\text{em}} = \frac{1}{2}\left(\frac{1}{\mu_0} \boldsymbol{B} \cdot \boldsymbol{B} + \epsilon_0 \boldsymbol{E} \cdot \boldsymbol{E}\right) \quad (14)$$

is the electromagnetic energy density and $\boldsymbol{S} = \boldsymbol{E} \times \boldsymbol{B}/\mu_0$ is the Poynting vector. The expression that accounts for these

changes is Poynting's theorem

$$\frac{\partial \varepsilon^{\mathrm{em}}}{\partial t} + \nabla \cdot \boldsymbol{S} + \boldsymbol{J} \cdot \boldsymbol{E} = 0. \tag{15}$$

Nevertheless, Equations (8) and (11) are exact in their description of the kinetic and thermal energy density transfer and transport, as well as the energy density exchange between fields and particles.

Before tackling the energy transfer problem, we explicitly define the following three terms, which are often used interchangeably in the literature:

1. *Heating* is any increase in $\varepsilon_s^{\mathrm{th}}$, and *cooling* is any decrease in $\varepsilon_s^{\mathrm{th}}$. Heating can be either reversible or irreversible.
2. *Damping* is any decrease in $\varepsilon^{\mathrm{em}}$, and *growth* is any increase in $\varepsilon^{\mathrm{em}}$. Damping/growth can be either reversible or irreversible.
3. *Dissipation* is any irreversible energy transfer leading to an increase in $\varepsilon_s^{\mathrm{th}}$.

Dissipation corresponds to an increase in entropy of the velocity distribution function, which is challenging to quantify directly both in space measurements and in simulations. Nonetheless, recent studies (Pezzi et al. 2019; Matthaeus et al. 2020; Pezzi et al. 2021) show that in collisionless plasmas energy-based dissipation proxies such as the Zenitani parameter (Zenitani et al. 2011)

$$D_{zs} = \boldsymbol{J} \cdot (\boldsymbol{E} + \boldsymbol{u}_s \times \boldsymbol{B}) - n_s q_s (\boldsymbol{u}_s \cdot \boldsymbol{E}), \tag{16}$$

and the strain pressure interaction $\nabla \boldsymbol{u}_s : \overline{\boldsymbol{P}}_s$ (Yang et al. 2017) are spatially correlated with dimensionless measures of nonthermal distribution functions (Kaufmann & Paterson 2009; Greco et al. 2012; Liang et al. 2019) and plasma agyrotropy (Scudder & Daughton 2008). In Equation (16), $\boldsymbol{J} = \sum_{s=i,e} q_s n_s \boldsymbol{u}_s$ is the electric current density.

These energy-based dissipation proxies are effectively power density terms derived from the left-hand sides of our Equations (8) and (11). According to our definitions, D_{zs} is a damping measure since it quantifies the energy transfer from the electromagnetic fields into bulk kinetic energy and vice versa.

The strain tensor interaction has gyrotropic and agyrotropic contributions. We decompose the pressure tensor as $P_{ij,s} = p_s \delta_{ij} + \Pi_{ij,s}$, where

$$p_s = \frac{1}{3} \sum_{i=1}^{3} P_{ii,s} \tag{17}$$

is the isotropic scalar pressure and

$$\Pi_{ij,s} = (P_{ij,s} + P_{ji,s})/2 - p_s \delta_{ij} \tag{18}$$

is the deviatoric pressure. Likewise, the strain rate tensor $\nabla \boldsymbol{u}_s$ can be expressed as $\nabla u_{ij,s} = \theta_s \delta_{ij}/3 + D_{ij,s}$, where $\theta_s = \nabla \cdot \boldsymbol{u}_s$ represents the dilatation term and

$$D_{ij,s} = \frac{1}{2}\left(\frac{\partial u_{i,s}}{\partial x_j} + \frac{\partial u_{j,s}}{\partial x_i}\right) - \frac{1}{3}\theta_s \delta_{ij} \tag{19}$$

represents the symmetric traceless strain rate tensor (Yang et al. 2017). Thus, the strain tensor interaction, which is a heating/cooling proxy according to our definitions, is

$$\nabla \boldsymbol{u}_s : \overline{\boldsymbol{P}}_s = p_s \theta_s + \Pi_{ij,s} D_{ij,s}, \tag{20}$$

where the first term on the right-hand side is known as $p\theta_s$ and the second term on the right-hand side is known as $Pi - D_s$ (Yang et al. 2017). For comparison with previous studies (Bandyopadhyay et al. 2020; Pezzi et al. 2021), in Section 3.6 we compute $D_{ij,s}$, $p_s\theta_s$, and $\Pi_{ij,s}D_{ij,s}$ and compare them with the energy transfer and transport terms, $-n_s q_s(\boldsymbol{u}_s \cdot \boldsymbol{E})$ and $\nabla \boldsymbol{u}_s : \overline{\boldsymbol{P}}_s$, in Equations (8) and (11).

3. Simulation Results

3.1. Simulation Setup

We use the explicit Plasma Simulation Code (PSC; Germaschewski et al. 2016) to simulate anisotropic Alfvénic turbulence in an ion−electron plasma in the presence of a constant background magnetic field $\boldsymbol{B}_0 = B_0 \hat{\boldsymbol{z}}$. The simulation domain is an elongated box of size $L_x \times L_y \times L_z = 24d_i \times 24d_i \times 125d_i$ with spatial resolution $\Delta x = \Delta y = \Delta z = 0.06 d_i$, where $d_i = c/\omega_{pi}$ is the ion inertial length, c is the speed of light, $\omega_{pi} = \sqrt{n_0 q_i^2/m_i \epsilon_0}$ is the ion plasma frequency, and n_0 is the constant initial ion density. The background ion Alfvén speed ratio in our simulations is $v_{A,i}/c = 0.1$, where $v_{A,i} = B_0/\sqrt{\mu_0 n_0 m_i}$ is the ion Alfvén speed. The number of macro particles per cell is 100 ions and 100 electrons. We use a mass ratio of $m_i/m_e = 100$ so that $d_e = 0.1 d_i$. We set the initial thermal-to-magnetic energy ratio $\beta_s = 2 n_0 \mu_0 k_{\mathrm{B}} T_s / B_0^2 = 1$, where T_s is the temperature of species s and k_{B} is the Boltzmann constant. The details of the simulation setup and the overall simulation results are presented by Agudelo Rueda et al. (2021), where the authors report a reconnection event that involves two reconnecting flux ropes.

3.2. Reconnection Event Overview

Panel (a) in Figure 1 shows the volume rendering of the current density in our simulation domain at the simulated time $t = 120 \omega_{pi}^{-1}$. Current filaments that form in the turbulent cascade are mostly elongated along the direction of the background magnetic field. At this time in the simulation, we apply the set of indicators presented by Agudelo Rueda et al. (2021) to identify and locate reconnection sites. We select one reconnection event that involves two reconnecting flux ropes as shown in panel (b) of Figure 1, where the magnetic field lines are color-coded with $|\boldsymbol{B}|$. The magnetic flux ropes contain an intense magnetic field, especially the lower flux rope, which is more twisted and has a smaller radius than the upper flux rope. Conversely, the magnetic field between the flux ropes is weak. The cuts in panel (b) show J_z in the x-y simulation plane. For our analysis of this event, we apply a 2D cut in the x-y plane at $z = 77 d_i$. Panel (c) of Figure 1 shows the magnetic field lines of the field components in the x-y plane, i.e., (B_x, B_y) as black contours. Panel (c) illustrates the complexity of the magnetic topology in the region of interest. For our energy analysis, we select a volumetric subregion of size $10 d_i^3$ centered around the identified reconnecting region. The green square in panel (c) highlights the intersection of the selected subregion with the central 2D cut from panel (b).

Even though the background field is in the z-direction, the current structures are not exactly aligned with the z-direction. Instead, the geometric features of the reconnection event are aligned with the plane perpendicular to the current sheet that sustains the magnetic gradient. Therefore, we determine a reference frame (RF) that is aligned with the main axis of the current sheet. We determine the direction of the main axis of
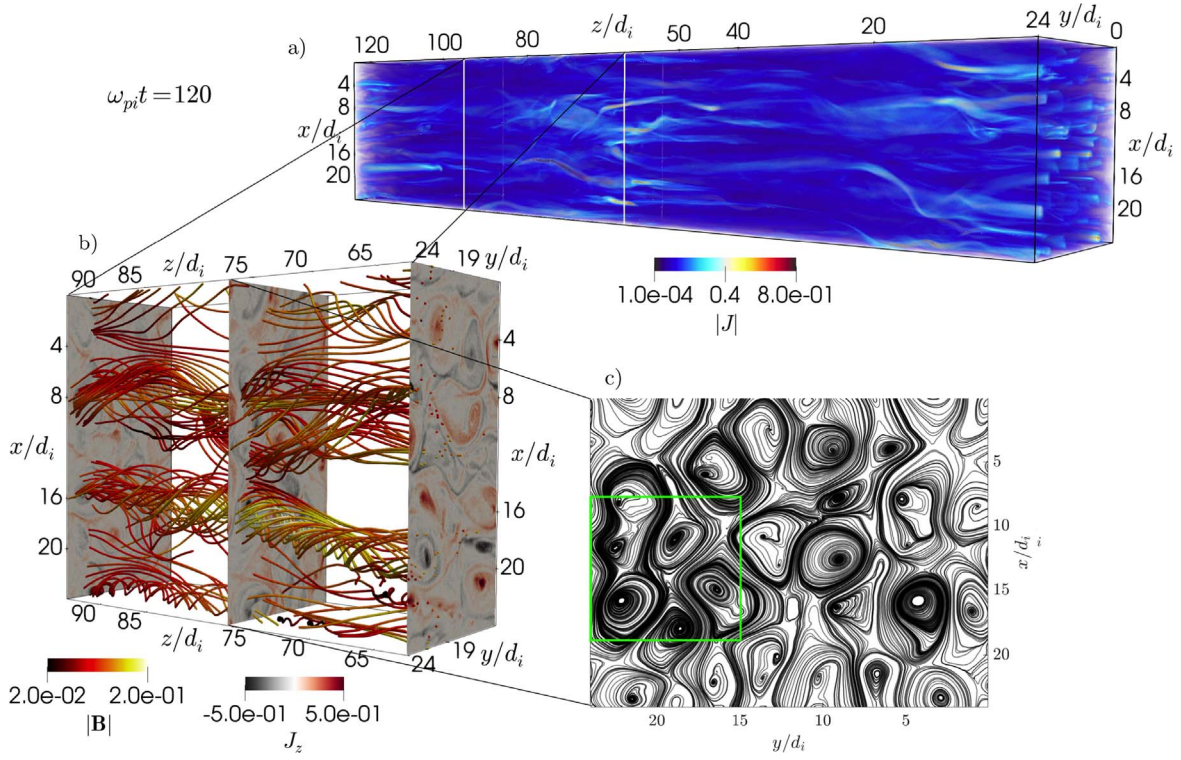
Figure 1. Spatial context of the reconnection event within the simulation domain. Panel (a) shows a volume rendering of $|\boldsymbol{J}|$. Panel (b) shows the 3D magnetic field lines color-coded with $|\boldsymbol{B}|$. On the vertical cuts in panel (b), we show J_z. Panel (c) shows the magnetic field lines in the x-y plane. The black contours show in-plane magnetic field lines. The green square highlights the size and position of the region for the energy analysis.
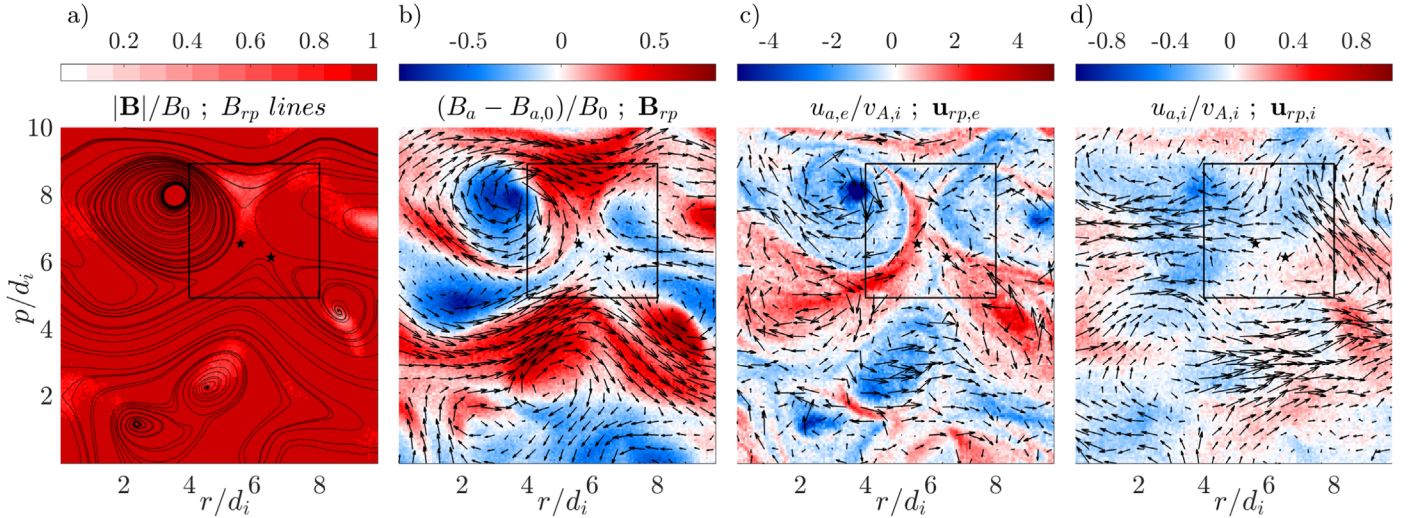
Figure 2. 2D cuts in the r-p plane at simulation time $t = 120\omega_{pi}^{-1}$. (a) Magnetic field magnitude $|\boldsymbol{B}|/B_0$. The black contours represent the in-plane magnetic field lines, and the black stars represent two x-points. (b) Out-of-plane component magnetic field $(B_a - B_{a,0})/B_0$. The black arrows in this panel represent the in-plane magnetic vectors ($\boldsymbol{B}_{rp}$). (c) Out-of-plane electron speed $u_{a,e}/v_{A,i}$. The black arrows in this panel represent the in-plane electron velocity vectors ($\boldsymbol{u}_{rp,e}/v_{A,i}$). (d) Out-of-plane ion speed $u_{a,i}/v_{A,i}$. The black arrows in this panel represent the in-plane ion velocity vectors ($\boldsymbol{u}_{rp,i}$). In all panels, the black square outlines the diffusion region.

the current sheet by 3D rendering J_z and measuring the inclination of the coherent structure that crosses the point $x = 13.5d_i$ and $y = 21.5d_i$ in the x-y plane. We then apply a coordinate transformation from the RF (x, y, z) to a new RF (r, p, a) aligned with the main axis of the current sheet. The unit vectors of this RF are $(\hat{\boldsymbol{r}}, \hat{\boldsymbol{p}}, \hat{\boldsymbol{a}})$. In this RF, $\hat{\boldsymbol{a}}$ is antiparallel to the main axis of the current sheet, $\hat{\boldsymbol{p}}$ is an arbitrary vector in

the plane perpendicular to $\hat{\boldsymbol{a}}$, and $\hat{\boldsymbol{r}}$ is the vector that completes the right-handed coordinate system. Since the components r and p are in the plane perpendicular to the current structure, we denote them as the in-plane components.

In the following analysis, we use the RF (r, p, a) and select a cubic region of size $10d_i^3$. Although the event is 3D and the magnetic field lines extend in three dimensions, we select a 2D

cut of the cubic region in the r-p plane similar to the green square in panel (c) of Figure 1. This 2D cut is representative of the reconnection event as we show in Section 3.3.

Panel (a) in Figure 2 shows the magnetic field magnitude in the region of interest normalized to B_0. The black contours represent the in-plane magnetic field lines, which we compute by creating an array of seed points placed on the vertices of a squared grid in the r-p plane. Then, we use the in-plane magnetic field vectors to create the streamlines. We propagate the numerical integration in both directions: forward and backward. Panel (b) in Figure 2 shows $(B_a - B_{a,0})/B_0$, where B_a is the out-of-plane component of the magnetic field and $B_{a,0} = \boldsymbol{B}_0 \cdot \hat{\boldsymbol{a}}$ is the projection of $\boldsymbol{B}_0$ on the a-direction. We subtract $B_{a,0}$ to improve the visibility of the multipolar configuration of this component. The black arrows in this panel represent the in-plane magnetic field vectors $\boldsymbol{B}_{rp} = B_r \hat{\boldsymbol{r}} + B_p \hat{\boldsymbol{p}}$. In order for reconnection to occur, the in-plane components of the magnetic fields of reconnecting structures must have different directions. The plotted in-plane magnetic field lines suggest the presence of effective separatrices between regions of opposite $\boldsymbol{B}_{rp}$ within the black square.

The in-plane magnetic field lines in panel (a), along with the direction of the in-plane magnetic field vectors, suggest the presence of two x-points, which we mark with two black stars, one located at $r = 5.58d_i$ and $p = 6.6d_i$ and the other at $r = 6.5d_i$ and $p = 6.2d_i$. We establish the position of the x-points by identifying the saddle points of the in-plane magnetic field. The magnetic configuration is complex, and the black square outlines the central region in which the reconnection occurs. Within this region, the magnetic field is nonuniform. The subregion where $|\boldsymbol{B}| \approx 0$ represents a null region. From now on, we refer to the region enclosing the x-points as the diffusion region. Since transverse 2D cuts to 3D magnetic flux ropes resemble the geometry of magnetic islands, we now refer to the magnetic field lines that are quasi-circular in panel (a) as magnetic islands.

Panel (c) shows the out-of-plane component of the electron velocity $u_{a,e}$ normalized to the ion Alfvén speed $v_{A,i}$. The red color indicates electrons moving out of the plane, whereas the blue color indicates electrons moving into the plane. The black arrows of this panel represent the in-plane electron velocity vectors $\boldsymbol{u}_{rp,e} = u_{r,e} \hat{\boldsymbol{r}} + u_{p,e} \hat{\boldsymbol{p}}$. Within the region of interest, there are counterstreaming electrons following the separatrices. Likewise, we locate electrons streaming out of the plane through the diffusion region. Within the magnetic islands, the electrons stream into the plane. In most of the magnetic islands, the electrons follow quasi-circular orbits owing to their magnetization. However, in the magnetic island centered at $r = 4.5d_i$ and $p = 2.2d_i$, the electrons demagnetize and traverse into the magnetic island connecting with the stream of electrons at the edge of the magnetic island.

Panel (d) shows the out-of-plane component of the ion velocity $u_{a,i}$ normalized to $v_{A,i}$. The black arrows in this panel represent the in-plane ion velocity vectors $\boldsymbol{u}_{rp,i} = u_{r,i} \hat{\boldsymbol{r}} + u_{p,i} \hat{\boldsymbol{p}}$. Within the diffusion region, the out-of-plane ion velocity is small, which suggests that the ion motion is mostly constrained to the plane. The in-plane motion, however, is considerable, and the ions move across the separatrices since they are demagnetized.

3.3. Particle Agyrotropy in the Diffusion Region

During the reconnection of magnetic flux ropes, the plasma expansion/contraction is not isotropic. Therefore, at kinetic scales, the plasma pressure of each species can develop anisotropy and agyrotropy. Figure 3 shows our pressure terms according to Equations (17) and (18) for electrons and ions normalized to $p_0 = n_0 m_i v_{A,i}^2$. Panels (a) and (e) show the isotropic scalar pressure for electrons p_e and ions p_i, respectively. For both species, the scalar pressure is greater inside the magnetic islands than outside owing to the large density of particles (not shown here). Likewise, p_e and p_i display gradients along and across the separatrices. We find that p_e is lower in the region between the magnetic islands and between the x-points compared to inside the magnetic islands.

Panels (b), (c), and (d) of Figure 3 show the off-diagonal components of the electron pressure tensor according to Equation (18), $\Pi_{ra,e}$, $\Pi_{pa,e}$, and $\Pi_{pr,e}$, respectively. We here introduce our notation $\langle ... \rangle$ for the spatial average of a quantity over a given domain. The averages over the subdomain of $|\Pi_{ra,e}|$, as well as $|\Pi_{pa,e}|$, and $\langle|\Pi_{ra,e}|\rangle$, and $\langle|\Pi_{pa,e}|\rangle$, are about 10% of $\langle p_e \rangle$. $\Pi_{ra,e}$ and $\Pi_{pa,e}$ present a strong dipole-like configuration centered on the magnetic islands. There is a shallower, yet visible, gradient in $\Pi_{ra,e}$, $\Pi_{pa,e}$, and $\Pi_{pr,e}$ in the region between the islands and in the diffusion region. Conversely, $\Pi_{pr,e}$ exhibits a quadrupolar configuration within the magnetic islands. The nonzero values of $\Pi_{ra,e}$, $\Pi_{pa,e}$, and $\Pi_{pr,e}$ show that the plasma is agyrotropic, suggesting that small-scale kinetic processes occur. Similar patterns are reported along the separatrices of 2D collisionless reconnection (Yin et al. 2001; Schmitz & Grauer 2006; Wang et al. 2015) and laminar 3D collisionless reconnection (Wang et al. 2018). However, unlike previous studies, we observe the same patterns within the magnetic islands of turbulent 3D magnetic reconnection. This is a fundamental difference between the reconnection that occurs in turbulence and steady-state reconnection that occurs in Harris current sheet configurations.

Panels (f), (g), and (h) of Figure 3 show the off-diagonal components of the ion pressure tensor according to Equation (18), $\Pi_{ra,i}$, $\Pi_{pa,i}$, and $\Pi_{pr,i}$, respectively. The off-diagonal terms for ions, unlike electrons, have a less coherent pattern attached to the in-plane magnetic field topology. The reason for this detachment lies in the demagnetization of the ions at these scales. Nevertheless, there is a gradient of these terms suggesting agyrotropy effects in the ion dynamics as well.

Figure 4 shows a magnification of the region enclosed by the black square in Figure 2. Panels (a)−(d) show a magnification of the electron pressure terms shown in panels (a)−(d) of Figure 3. To make a direct comparison with previous 2D studies, panels (e)−(h) show sketches summarizing known patterns associated with the electron pressure components that emerge from 2D collisionless reconnection in the absence of a guide field (Yin et al. 2001; Schmitz & Grauer 2006; Wang et al. 2015). In this region, unlike within the magnetic islands of Figure 3, our simulation results of the electron pressure patterns match those patterns shown in the sketches in panels (e)−(h) in the region where the magnetic field has a local minimum according to panel (a) in Figure 1. However, below the x-point located at $r = 5.58d_i$ and $p = 6.6d_i$, the pattern no longer corresponds to the sketched expectations. Moreover, $\Pi_{pr,e}$ is less coherent, and we do not recognize a clear quadrupolar configuration as in the sketches for the 2D case.
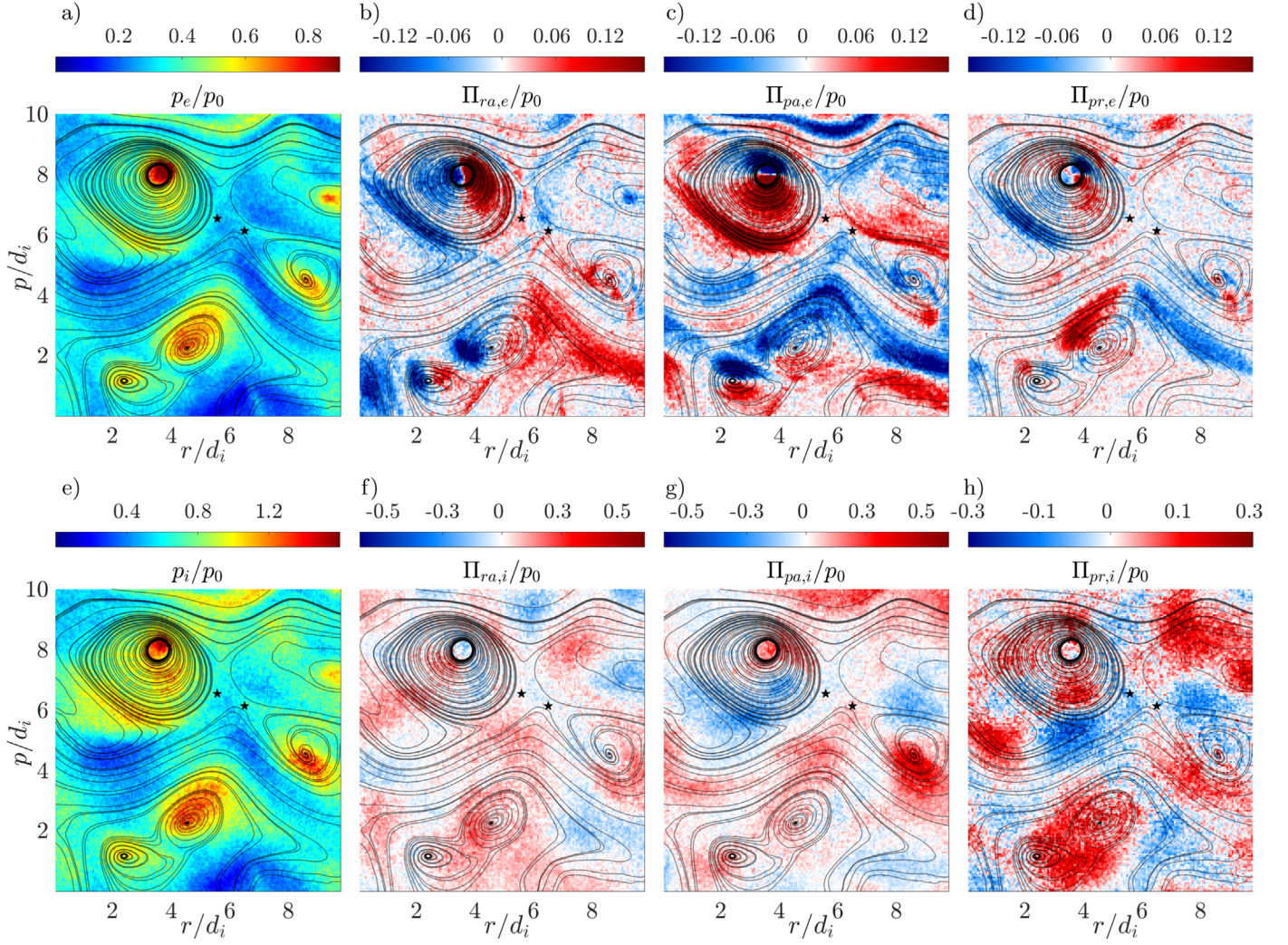
Figure 3. 2D cuts of the pressure tensor components in the r-p plane at the simulation time $t = 120\omega_{pi}^{-1}$. (a) Electron scalar pressure p_e/p_0. Off-diagonal components of the electron pressure tensor: (b) $\Pi_{ra,e}/p_0$, (c) $\Pi_{pa,e}/p_0$, and (d) $\Pi_{pr,e}/p_0$. (e) Ion scalar pressure p_i/p_0. Off-diagonal components of the ion pressure tensor: (f) $\Pi_{ra,i}/p_0$, (g) $\Pi_{pa,i}/p_0$, and (h) $\Pi_{ra,i}/p_0$.

Figure 5 shows a 3D representation of the pressure components for electrons in panels (a)−(d) and for ions in panels (e)−(h). The 2D cut at $a = 2.76d_i$ corresponds to the 2D cut in Figure 3. The plotted 3D structures are isosurfaces of the pressure component depicted on the 2D planes. For a given quantity ψ, the value of the isosurfaces corresponds to $S_\psi = \pm(\langle|\psi|\rangle + 2\sigma_{|\psi|})$, where $\sigma_{|\psi|}$ is the standard deviation of $|\psi|$. The isosurfaces in panels (a)−(h) have the shape of elongated and thin surfaces with local curvatures along the a-axis. The agyrotropic patterns in Figure 3 extend for $\sim5d_i$ along the a-axis.

3.4. Energy Transfer and Transport

We use the power density expressions for the kinetic energy in Equation (8) and the thermal energy in Equation (11) to describe the energy transfer and transport associated with our reconnection event. To compute the partial time derivatives of a quantity, we use a central difference approach. Since the Alfvén transit time is $\sim100\ \omega_{pi}^{-1}$, a time resolution of $6\ \omega_{pi}^{-1}$ is sufficient to capture the relevant dynamics of interest. To estimate the spatial derivatives, we use a standard cell-centered first-neighbors approach. We calculate all scalar products cell-

wise in the simulation domain. Panels (a)−(e) of Figure 6 show 2D cuts of each term in Equation (8) for electrons normalized to $\Delta\varepsilon_0 = \omega_{pi}m_i v_{A,i}^2$.

Panel (a) shows, at the simulation time $t = 120\omega_{pi}^{-1}$, the total time derivative of the kinetic energy density $d\varepsilon_e^k/dt$. The domain exhibits considerable temporal changes of the kinetic energy density at the centers of the magnetic islands. We also detect negative $d\varepsilon_e^k/dt$ at the edge of the top left magnetic island and positive $d\varepsilon_e^k/dt$ in the diffusion region. Conversely, there is almost no change in $\varepsilon_e^{\rm th}$ in the region between the x-points.

Panel (b) shows the scalar product $\boldsymbol{u}_e \cdot \nabla \cdot \overline{\boldsymbol{P}}_e$, which quantifies the change of kinetic energy due to the advection of the pressure tensor. This energy change is transported by the electron flow. The quantity $\boldsymbol{u}_e \cdot \nabla \cdot \overline{\boldsymbol{P}}_e$ is also known as the pressure work (Fadanelli et al. 2021). There is a strong conversion of energy associated with the pressure work at the center of the magnetic islands. However, the energy change associated with this term is around 10 times greater than the local $d\varepsilon_e^k/dt$. Unlike $d\varepsilon_e^k/dt$, at the edge of the top left magnetic island, there is a strong gradient of $\boldsymbol{u}_e \cdot \nabla \cdot \overline{\boldsymbol{P}}_e$ from
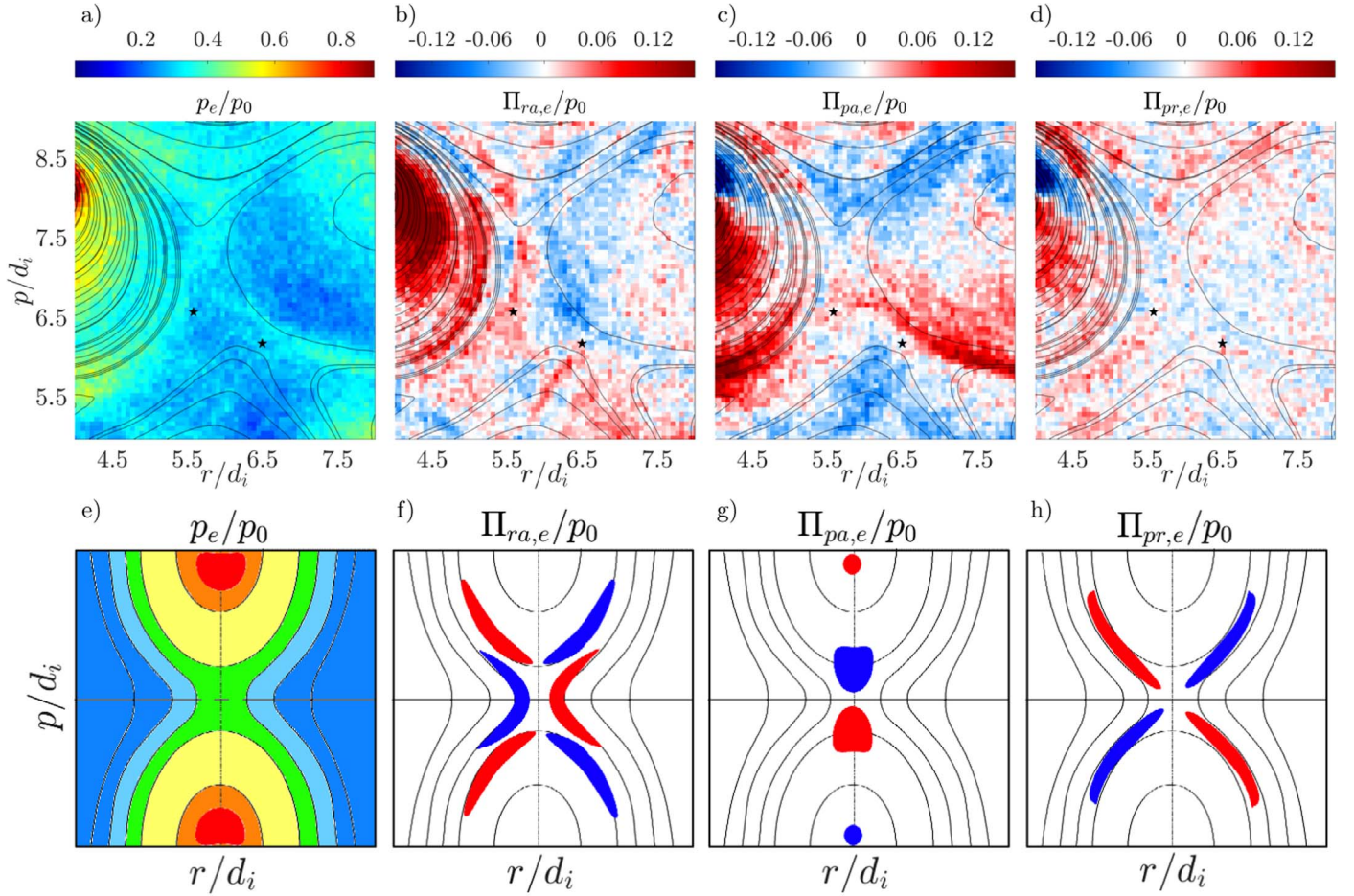
Figure 4. Magnification of the region delimited by the black square in Figure 2 in the r-p plane at the simulation time $t = 120\omega_{pi}^{-1}$. (a) Electron scalar pressure p_e. Off-diagonal components of the electron pressure tensor: (b) $\Pi_{ra,e}$, (c) $\Pi_{pa,e}$, and (d) $\Pi_{pr,e}$. Panel (e) shows a sketch of the patterns of the scalar pressure emerging in 2D simulations of reconnection, and panels (f)−(h) show sketches of the off-diagonal terms of the electron pressure based on 2D Harris current sheet reconnection without a guide field (Yin et al. 2001).

the left-hand side of the magnetic island to the right-hand side. In addition, $\boldsymbol{u}_e \cdot \nabla \cdot \overline{\boldsymbol{P}}_e$ has a local minimum in the region between the x-points.

Panel (c) shows $\varepsilon_e^k \nabla \cdot \boldsymbol{u}_e$, which represents the kinetic energy change due to divergent or convergent flow patterns in the electron bulk velocity. Like for the previous terms, $\varepsilon_e^k \nabla \cdot \boldsymbol{u}_e$ is greater at the center of the magnetic islands than in the region between them. There is no noticeable gradient of this term between the x-points. Although panels (a), (b), and (c) show similar patterns in their signs, there are local differences, especially in the diffusion region.

Panel (d) shows $- q_e n_e (\boldsymbol{u}_e \cdot \boldsymbol{E})$, which represents the energy exchange between the electrons and the electric field. We find a considerable energy conversion not only within the magnetic islands but also in the region between the islands, as well as in the region between the x-points. In the region between the x-points, the electrons gain kinetic energy from the electric field. Along the separatrix next to the top left island, the electron bulk motion is decelerated by the electric field. Comparing panels (b) and (d), $\boldsymbol{u}_e \cdot \nabla \cdot \overline{\boldsymbol{P}}_e$ and $- q_e n_e (\boldsymbol{u}_e \cdot \boldsymbol{E})$ balance with each other in the diffusion region.

Panel (e) shows Ξ_s^k, which we compute as the sum of all terms on the left-hand side of Equation (8). There are regions with positive and negative Ξ_e^k within the magnetic islands. On

the contrary, Ξ_e^k is predominately positive within the diffusion region and along the separatrices.

Although we do not include binary collisions in our code explicitly, we acknowledge that the finite number of macroparticles affects the system in a way similar to collisions and leads to an undersampling of nonthermal fine structure in the velocity distribution function, which generates a loss of information and thus increase in entropy.

In a real plasma, binary collisions between particles drive the system to a thermal equilibrium, thus smoothing out the distribution function. Similarly, a finite number of particles represents a low number of counts to compute the statistical measures. Therefore, when computing macroscopic quantities, the contribution from nonthermal particles is overshadowed by the core distribution. It is effectively a coarse-graining effect, similar to the actual effect of collisions, albeit on a different timescale. However, this effect occurs earlier in PIC simulations with a finite number of particles than in the real solar wind. We conjecture that the impact is ultimately comparable.

Panels (f)−(j) of Figure 6 show 2D cuts of each term in Equation (11) normalized to $\Delta\varepsilon_0$. Panel (f) depicts $d\varepsilon_e^{\mathrm{th}}/dt$. As in the kinetic energy case, $d\varepsilon_e^{\mathrm{th}}/dt$ has local extrema associated with the magnetic islands. The main change in $d\varepsilon_e^{\mathrm{th}}/dt$ is due to the advective term $(\boldsymbol{u}_e \cdot \nabla)\varepsilon_e^{\mathrm{th}}$. By direct comparison with panel
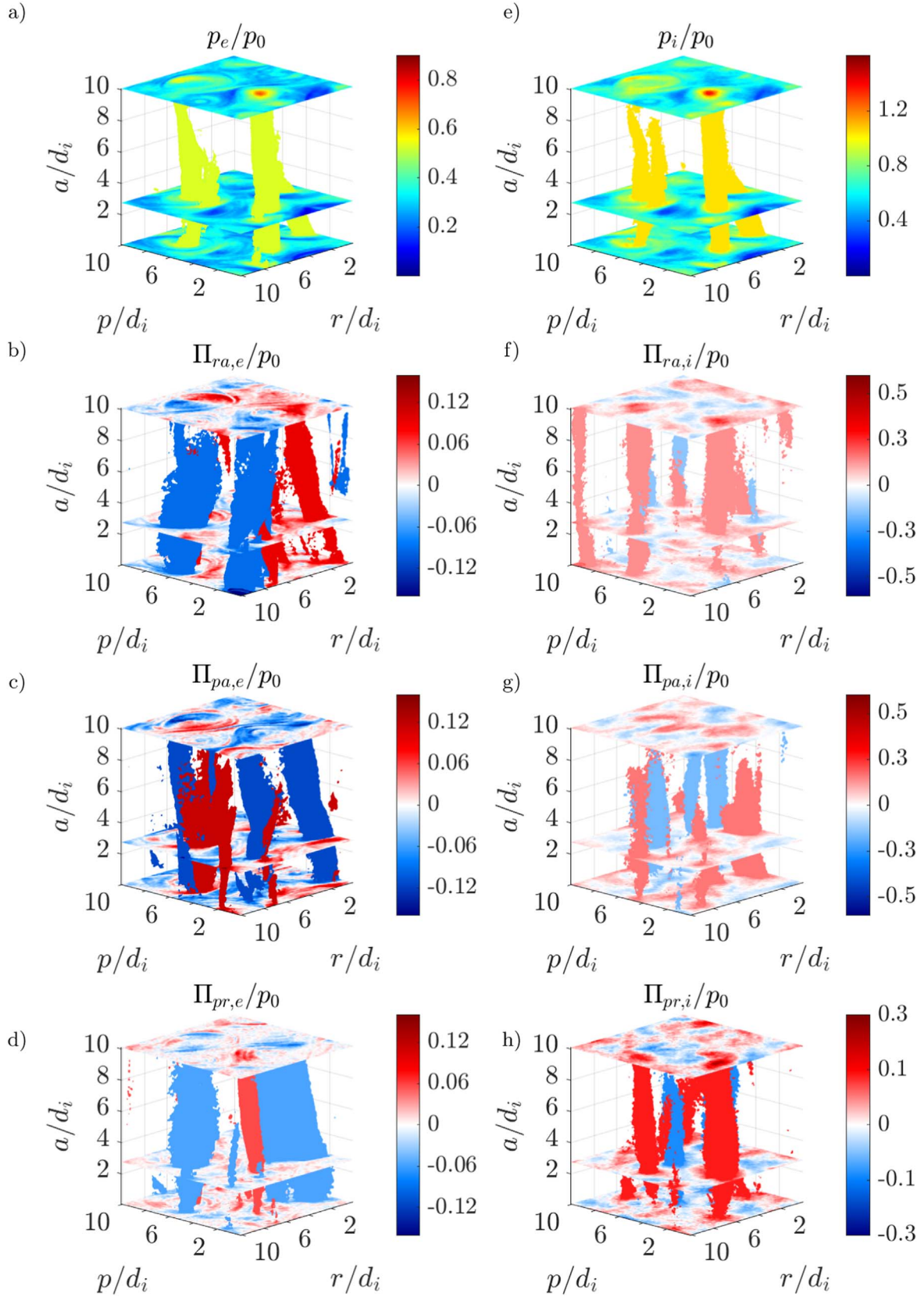
Figure 5. 2D cuts in the *r*-*p* plane and isosurfaces of the pressure tensor components at the simulation time $t = 120\omega_{pi}^{-1}$. (a) Electron scalar pressure p_e/p_0. Off-diagonal components of the electron pressure tensor: (b) $\Pi_{ra,e}/p_0$, (c) $\Pi_{pa,e}/p_0$, and (d) $\Pi_{pr,e}/p_0$. (e) Ion scalar pressure p_i/p_0. Off-diagonal components of the ion pressure tensor: (f) $\Pi_{ra,i}/p_0$, (g) $\Pi_{pa,i}/p_0$, and (h) $\Pi_{ra,i}/p_0$.
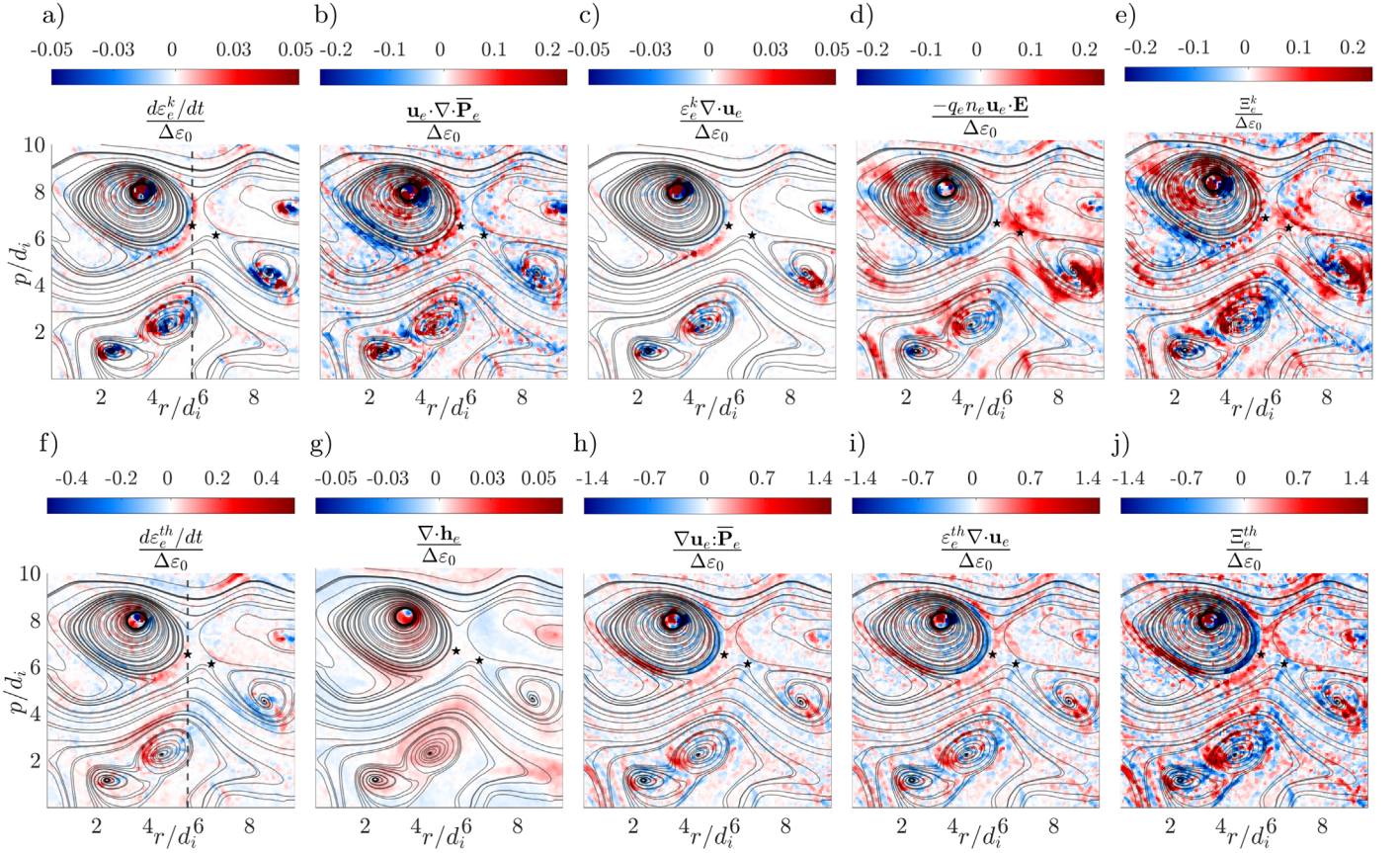
Figure 6. 2D cuts in the *r-p* plane at the simulation time $t = 120\omega_{pi}^{-1}$. (a−e) Kinetic power density terms for electrons. (f−j) Thermal power density terms for electrons. All quantities are normalized to $\Delta\varepsilon_0 = \omega_{pi} m_i v_{A,i}^2$. The vertical dashed lines in panels (a)−(f) show the 1D trajectory for our 1D analysis.

(b), we note similar power density patterns between $d\varepsilon_e^{\text{th}}/dt$ and $\boldsymbol{u}_e \cdot \nabla \cdot \overline{\boldsymbol{P}}_e$.

For the heat flux term $\nabla \cdot \boldsymbol{h}_e$, we do not directly compute $\nabla \cdot \boldsymbol{h}_e$ as a particle moment but use a Hammett−Perkins approach (Hammett & Perkins 1990) to estimate its contribution. This approach has been successfully applied in previous collisionless reconnection studies (Ng et al. 2015; Wang et al. 2015; Ng et al. 2017). In this framework, we estimate

$$\nabla \cdot \boldsymbol{h}_e \approx v_e^{\text{th}} \frac{1}{2} |k_0| \, Tr[P_{ij,e} - \langle P_{ij,e} \rangle - \delta_{ij}(n_e - \langle n_e \rangle)\langle T_e \rangle], \tag{21}$$

where $v_e^{\text{th}} = \sqrt{2k_{\text{B}} T_e / m_e}$ is the thermal speed of the electrons. The wavenumber $k_0 = \sqrt{3}/|L_s|$ is a representative wavenumber associated with a subdomain of volume $V_s = L_s^3$, where $L_s = 10.08 d_i$, which we select as the region to study the energy conversion during the reconnection event. Panel (g) shows our estimation of $\nabla \cdot \boldsymbol{h}_e$. There is a positive power density contribution from particle heat flux inside the magnetic islands. Conversely, there is a negative contribution in the regions between the magnetic islands.

Panel (h) depicts the collisionless energy transfer $\nabla \boldsymbol{u}_e : \overline{\boldsymbol{P}}_e$ between kinetic and thermal energies. This term has contributions from the diagonal elements of the tensors that are associated with the isotropic energy transport and from the off-diagonal elements that quantify the agyrotropy in the plasma. There is positive $\nabla \boldsymbol{u}_e : \nabla \overline{\boldsymbol{P}}_e$ in the region between the magnetic islands that is associated with counterstreaming electrons. We

locate an *x*-like structure centered in the region where the magnetic field strength exhibits a local minimum. In the region between the *x*-points, as well as to the left of the diffusion region, $\nabla \boldsymbol{u}_e : \overline{\boldsymbol{P}}_e < 0$.

Panel (i) shows the thermal energy transport $\varepsilon_e^{\text{th}} \nabla \cdot \boldsymbol{u}_e$ associated with the compression/expansion of the electron flow. At first glance, the positive/negative patterns in $\varepsilon_e^{\text{th}} \nabla \cdot \boldsymbol{u}_e$ seem very similar to the patterns in $\nabla \boldsymbol{u}_e : \overline{\boldsymbol{P}}_e$. The reason for this similarity is that the main energy transport in $\nabla \boldsymbol{u}_e : \overline{\boldsymbol{P}}_e$ is associated with the contribution of diagonal elements as we show in Section 3.6. However, we find local differences due to the agyrotropic contributions. From all terms on the left-hand sides of Equations (8) and (11), only the terms associated with the strain tensor present an extended asymmetric *x*-point-like structure in the diffusion region. Comparing panels (c) and (i), $\varepsilon_e^{\text{th}} \nabla \cdot \boldsymbol{u}_e$ is on average larger and forms broader structures than $\varepsilon_e^k \nabla \cdot \boldsymbol{u}_e$.

Panel (j) shows Ξ_s^{th}, which we compute as the sum of all terms on the left-hand side of Equation (11). This energy transfer is significant, as the different terms on the left-hand side of Equation (11) do not add up to zero.

In Figure 7, we show vertical 1D cuts of the power density terms along the *p*-direction at $r = 5.58 d_i$ to visualize the relation between the different terms for plasma electrons. We further show a magnification of the region delimited by the black square from Figure 2. Panel (a) shows the kinetic power density terms in Equation (8). We observe that the fluctuations in $d\varepsilon_e^k/dt$ (green line) and $\varepsilon_e^k \nabla \cdot \boldsymbol{u}_e$ (black line) are negligible
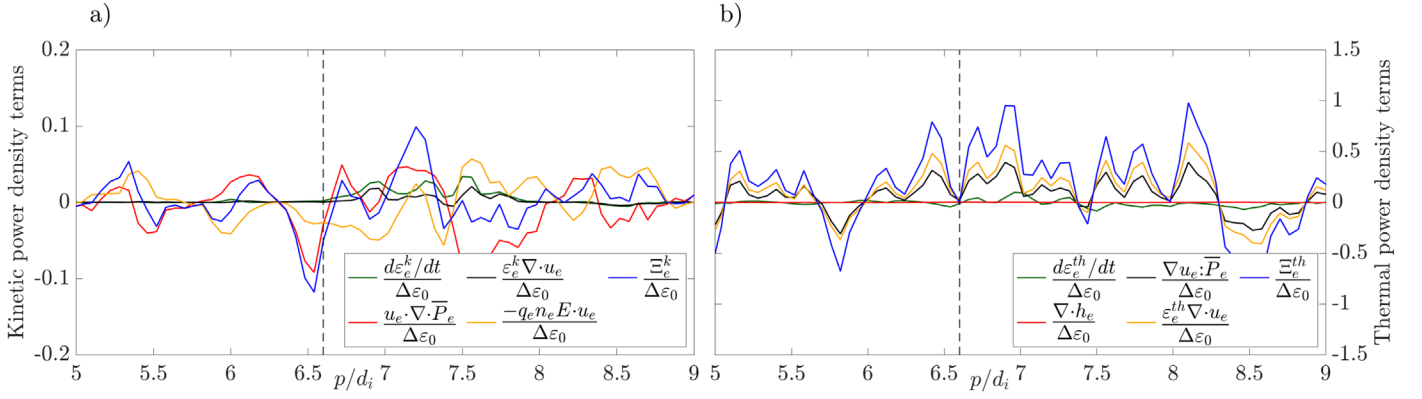
Figure 7. 1D cuts of the power density terms along the $\hat{p}$-direction at $r = 5.58d_i$ and at the simulation time $t = 120\omega_{pi}^{-1}$. (a) Kinetic power density terms in Equation (8). (b) Thermal power density terms in Equation (11). The vertical dashed line represents the crossing of the x-point at $r = 5.58d_i$ and $p = 6.6d_i$.

compared with $\boldsymbol{u}_e \cdot \nabla \cdot \overline{\boldsymbol{P}}_e$ (red line) and $-q_e n_e \boldsymbol{E} \cdot \boldsymbol{u}_e$ (yellow line). However, there is a noticeable disturbance in all quantities in the range $p = 6.96d_i-7.84d_i$, which is located in the region of the diffusion region at which the magnetic field is nearly zero. Along the 1D cut, $\boldsymbol{u}_e \cdot \nabla \cdot \overline{\boldsymbol{P}}_e$ and $-q_e n_e \boldsymbol{E} \cdot \boldsymbol{u}_e$ are anticorrelated. This anticorrelation breaks when the disturbances in $d\varepsilon_e^k/dt$ and $\varepsilon_e^k \nabla \cdot \boldsymbol{u}_e$ occur. For this panel, the curve of Ξ_s^k (blue line) changes sign when crossing the x-point.

Panel (b) shows the thermal power density terms in Equation (11). Comparing panels (a) and (b), we observe that the fluctuations in the thermal power density terms are more pronounced than those in the kinetic power density. In panel (b), the fluctuations in $d\varepsilon_e^{th}/dt$ (green line) and $\nabla \cdot \boldsymbol{h}_e$ (red line) are negligible compared with $\nabla \boldsymbol{u}_s : \overline{\boldsymbol{P}}_e$ (black line) and $\varepsilon_e^{th} \nabla \cdot \boldsymbol{u}_e$ (yellow line). Unlike in the kinetic power density case, the contributions from all terms in Equation (11) are either positive or negative at the same location, showing no anticorrelation between the dominant terms. We note that Ξ_e^{th} (blue line), unlike Ξ_e^k, is positive on both sides of the x-point.

Figure 8 shows a 3D representation of the kinetic power density terms in panels (a)−(d) and of thermal power density terms in panels (e)−(h). The 2D cut at $a = 2.76d_i$ corresponds to the 2D cuts in Figure 6. The plotted 3D structures are isosurfaces of the power density terms depicted on the 2D planes. Panels (a)−(d) show that the isosurfaces of $d\varepsilon_e^k/dt$, $\boldsymbol{u}_e \cdot \nabla \cdot \overline{\boldsymbol{P}}_e$ and ε_e^k are mostly thin filaments, whereas the isosurfaces of $-q_e n_e \boldsymbol{u}_e \cdot \boldsymbol{E}$ consist of broad patches. Moreover, there are more regions with $-q_e n_e \boldsymbol{u}_e \cdot \boldsymbol{E} > 0$ than with $-q_e n_e \boldsymbol{u}_e \cdot \boldsymbol{E} < 0$. Panels (e) and (f) show that the isosurfaces of $d\varepsilon_e^{th}/dt$ and $\nabla \cdot \boldsymbol{h}_e$ are also filamentary. Conversely, panels (g) and (h) show that the isosurfaces of $\boldsymbol{u}_s : \overline{\boldsymbol{P}}_e$ and $\varepsilon_e^{th} \nabla \cdot \boldsymbol{u}_e$ are mainly thin sheets.

Figure 9 depicts isosurfaces of Ξ_e^k in panel (a) and Ξ_e^{th} in panel (b). The most evident isosurface of Ξ_e^k is a filament located within the reconnecting flux rope. Conversely, the isosurfaces of Ξ_e^{th} are mostly thin sheets connected to the flux ropes.

3.5. Time Evolution

PIC simulations are affected by finite particle size, finite number of particles, and numerical integration errors that are effectively "collisional" contributions since they generate

phase-space particle diffusion (Hockney 1971; Dawson 1983; Klimontovich 2013; Birdsall & Langdon 2018; Grošelj 2019). Although the right-hand sides of the power density relations in Equations (8) and (11) include the contributions from numerical sources such as round-off errors and numerical heating, they also include contributions from the averaged, secular (including quasi-linear) correlations between fields and the particle distribution functions (Klein & Howes 2016; Howes et al. 2017; Klein et al. 2017). As shown by the field–particle correlation method, meaningful averages of the nonlinear correlations between the fluctuating electric field and the fluctuating perturbation of the distribution function define the secular transfer of energy from the fields to the particles. Thus, even in a purely collisionless plasma, the right-hand sides of Equations (8) and (11), after suitable averaging, are not exactly zero. In this interpretation, the averaging over higher-order field–particle correlations introduces irreversibility and thus dissipation into the kinetic description. All PIC systems share this behavior with statistical particle systems in reality.

In this section, we present a time evolution analysis of the energy density terms in order to estimate the nature of Ξ_s^k and Ξ_s^{th}. Figure 10(a) shows the time evolution of the energy densities averaged over the full simulation domain (solid curves, subscript "full") and averaged over the subdomain (dashed curves, subscript "sub"). The curves are normalized to $\varepsilon_0 = m_i v_{A,i}^2$. The total energy density is $\varepsilon^T = \varepsilon_e^k + \varepsilon_i^k + \varepsilon_e^{th} + \varepsilon_i^{th} + \varepsilon^{em}$. The averaged total energy densities $\langle \varepsilon_{full}^T \rangle$ and $\langle \varepsilon_{sub}^T \rangle$ (green curves) remain approximately constant. This suggests that numerical heating is negligible in our energy balance.

The thermal energy densities of both the ions (black curves) and the electrons (magenta curves) are greater than the kinetic energy densities of both the ions (yellow curves) and electrons (red curves). When averaged over the subdomain, the energy densities present more variability due to the inflowing and outflowing of energy density through the boundaries of the subdomain. Nevertheless, the time evolution of the quantities ε_{full} and ε_{sub} is approximately comparable.

Figure 10(b) depicts the time evolution of the absolute values of the energy density rates $\Delta\langle\varepsilon\rangle/\Delta t$ (dashed curves) and the dissipative power density rates Ξ (solid curves with circles), now averaged over the full simulation domain and normalized to ε_{full}^T. The time difference $\Delta t = 6\omega_{pi}^{-1}$ is the difference between two consecutive output times of our simulation.

As shown in panel (b), in the case of the ions, the thermal energy density rate (black dashed curve) and the kinetic energy
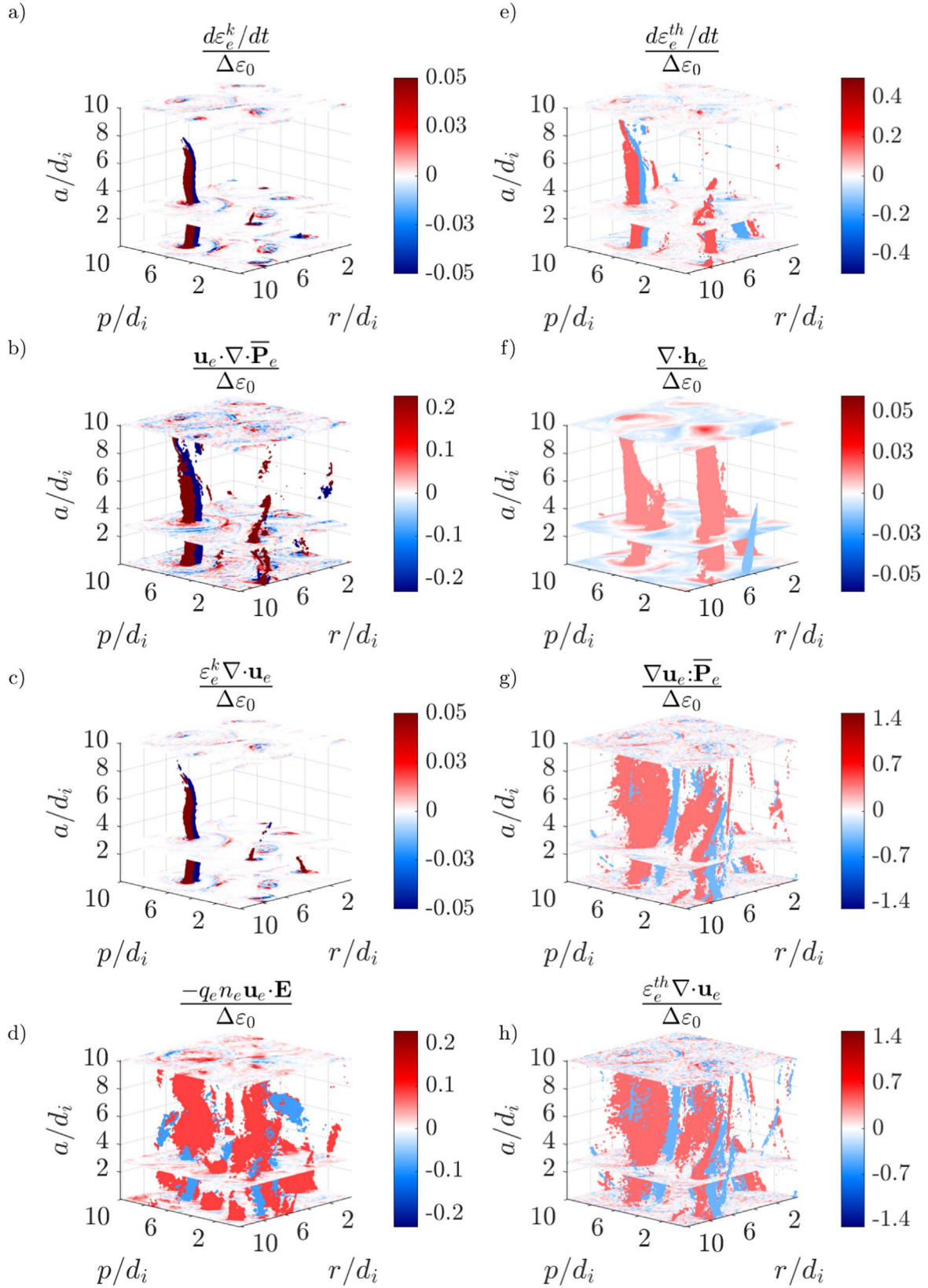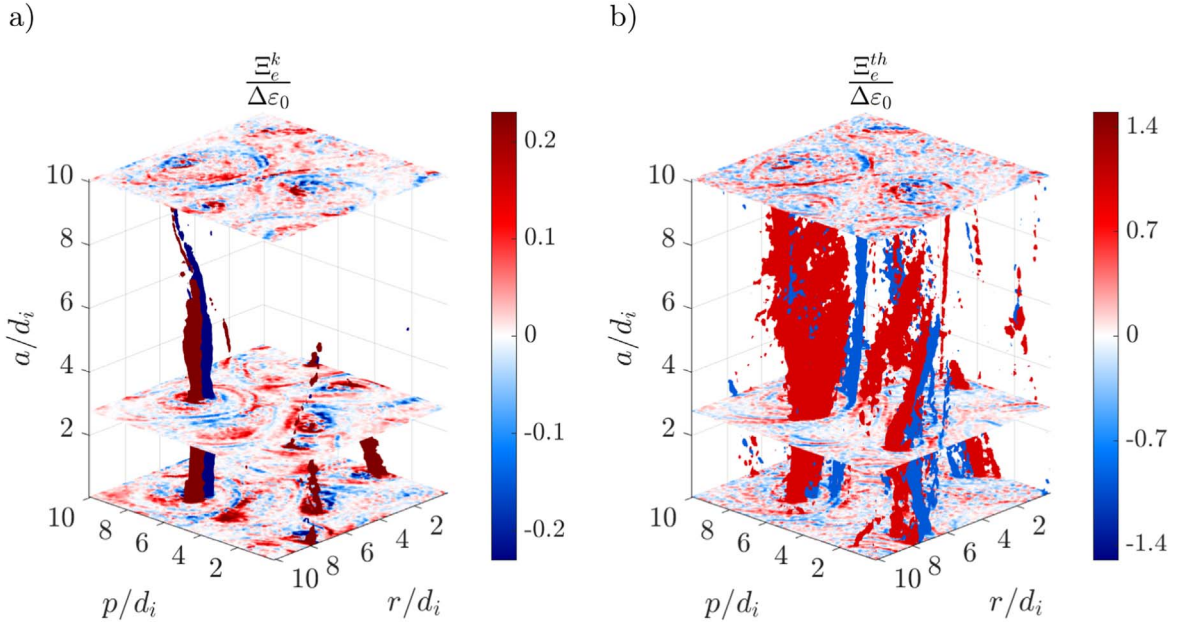
Figure 8. 2D cuts in the *r-p* plane and isosurfaces of the power density terms at the simulation time $t = 120\omega_{pi}^{-1}$. (a−e) Kinetic power density terms for electrons. (f−j) Thermal power density terms for electrons. All quantities are normalized to $\Delta\varepsilon_0 = \omega_{pi} m_i v_{A,i}^2$.

density rate (yellow dashed curve) are greater than the dissipative power density terms Ξ_i^{th} (black solid curve with circles) and Ξ_i^k (yellow solid curve with circles). The same

ordering applies to the electron case in which the thermal energy density rate (magenta dashed curve) and kinetic energy density rate (red dashed curve) are greater than Ξ_e^k (red solid

a)   b)

Figure 9. 2D cuts in the r-p plane and isosurfaces at the simulation time $t = 120\omega_{pi}^{-1}$. (a) Kinetic power density dissipation Ξ_e^k. (b) Thermal power density dissipation Ξ_e^{th}. All quantities are normalized to $\Delta\varepsilon_0 = \omega_{pi} m_i v_{A,i}^2$.

curve with circles) and Ξ_e^k (magenta solid curve with circles). For both species, $\Delta\varepsilon^{th}$ increases faster than $\Delta\varepsilon^k$.

During the initial phase of the simulation ($t\omega_{pi} \lesssim 100$), we find that $\langle \Xi_e^k \rangle > \langle \Xi_e^{th} \rangle$ when averaged over the full simulation domain. Afterward, for $t\omega_{pi} \gtrsim 100$, we find that $\langle \Xi_e^k \rangle < \langle \Xi_e^{th} \rangle$ when averaged over the full simulation domain until the simulation ends. The time $t\omega_{pi} \approx 100$ corresponds to the moment at which the overall J^{rms} reaches its global maximum in our simulation and significant magnetic reconnection sets in (Agudelo Rueda et al. 2021).

The total energy density rate $\Delta\varepsilon_{full}^T$ (green dashed curve) is lower than $\Delta\varepsilon^k$ and $\Delta\varepsilon^{th}$ for both species. Moreover, $\langle \Xi_e^{th} \rangle$ and $\langle \Xi_e^k \rangle$ are negligible compared with the kinetic and thermal energy density rates. This suggests that any irreversible energy transfer and thus numerical heating are negligible for the energy balance in our simulation. However, Ξ_e^{th} and Ξ_e^k are locally important near the reconnection region; see Figure 7.

3.6. Comparison with Damping and Heating Proxies

In recent studies (Yang et al. 2017; Pezzi et al. 2019; Matthaeus et al. 2020; Pezzi et al. 2021), the collisionless energy dissipation problem is tackled by studying quantities such as the Zenitani parameter defined in Equation (16) and the strain pressure interaction defined in Equation (20). We also explore these damping and heating proxies for comparison with our methods. Figure 11 depicts 2D cuts in the r-p plane and 1D cuts of these damping and heating proxies. Panel (a) shows D_{ze}. Similar to our kinetic and thermal power density terms, the magnetic islands present strong variations of D_{ze}. On the contrary, in the diffusion region, we see a coherent positive D_{ze} signature.

Panel (b) shows $p\theta_e$. The positive/negative patterns of this quantity are almost identical to our patterns of $\nabla u_e : \overline{P}_s$ (panel (h)) in Figure 6. This similarity illustrates that the main contribution to the strain tensor interaction comes from the diagonal elements of the strain tensor.

Panel (c) shows $Pi - D_e$. Although the positive/negative patterns in $Pi - D_e$ are similar to those in $p\theta_e$, $Pi - D_e$ presents clear differences, especially near the null region, where $Pi - D_e$ has the opposite sign of $p\theta_e$ along the separatrices. Moreover, along the separatrices, $|Pi - D_e| > D_{ze}$ and they share the same sign, whereas in the region between the x-points $Pi - D_e < 0$ and $D_{ze} > 0$.

Panel (d) shows 1D cuts of D_{ze} (blue line), $p\theta_e$ (red line), and $Pi - D_e$ (black line). We find that $p\theta_e$ is highly variable and, on average, greater than D_{ze} and $Pi - D_e$. This is considerably different compared with the Harris current sheet case (Pezzi et al. 2021), in which D_{ze} is the dominant energy transfer proxy. However, this behavior is consistent with turbulent simulations (Pezzi et al. 2021) and with observations of turbulent reconnection (Bandyopadhyay et al. 2021).

4. Discussion

The type of magnetic reconnection that occurs from a turbulent cascade (Servidio et al. 2010; Loureiro & Boldyrev 2020; Agudelo Rueda et al. 2021; Fadanelli et al. 2021) presents a more complex geometry of the diffusion region compared to its laminar counterpart. Likewise, the geometry of the regions with enhanced energy transport and transfer is more complex. Moreover, in a 3D geometry, the particle motion along the out-of-plane direction allows energy transfer that a 2D geometry precludes. For instance, the agyrotropic patterns in magnetic islands of 2D reconnection (Scudder & Daughton 2008) are located in the diffusion region outside the magnetic islands. Conversely, in our 3D case, we observe agyrotropic patterns in the cross section of the flux ropes, which we call magnetic islands.

Since the plasma density is greater in the centers of the magnetic islands, these regions exhibit a greater plasma pressure compared to outside the islands. Patterns of agyrotropic plasma pressure are present not only within the magnetic islands but also in the regions between them (Figure 3).
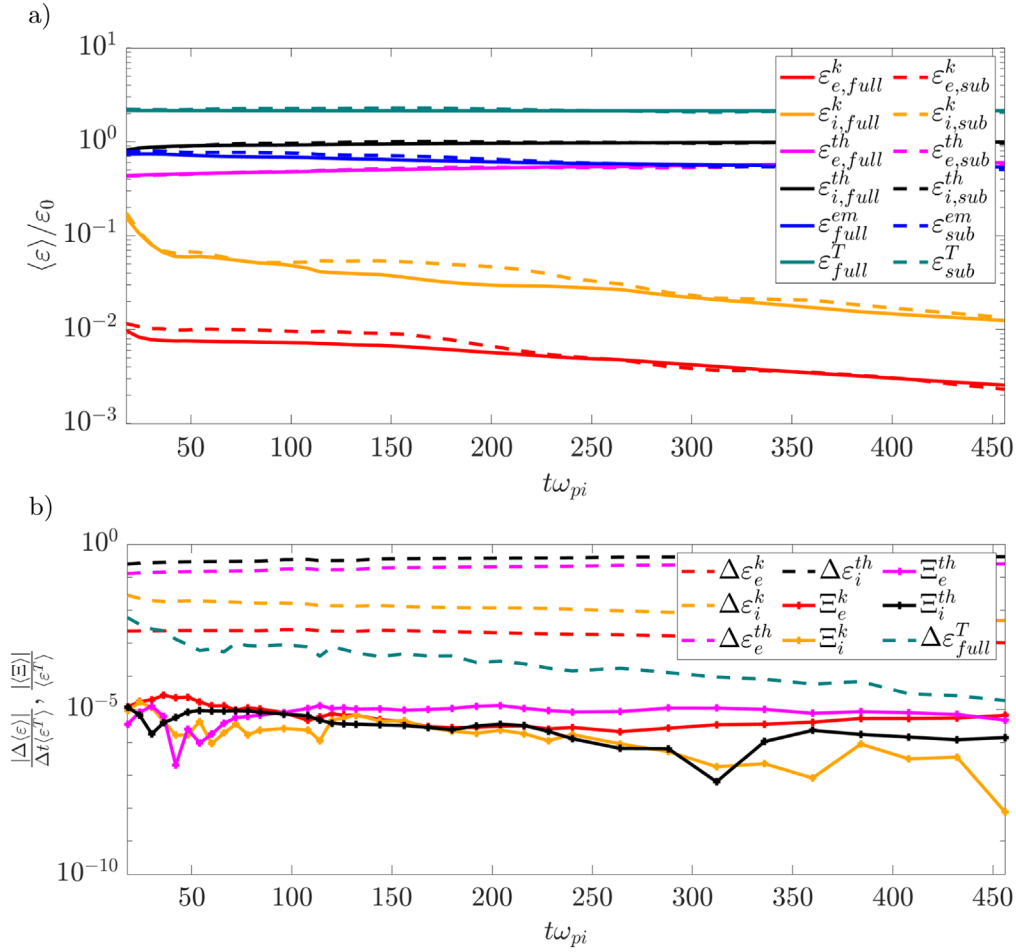
Figure 10. (a) Time evolution of the energy densities averaged over the full simulation domain (solid curves) and over the subdomain (dashed curves). The total energy density is $\varepsilon^T = \varepsilon_e^k + \varepsilon_i^k + \varepsilon_e^{th} + \varepsilon_i^{th} + \varepsilon^{em}$. (b) Time evolution of the absolute values of the energy density rates $\Delta\langle\varepsilon\rangle/\Delta t$ (dashed curves) and the dissipative power densities Ξ (solid curves with circles), averaged over the full simulation domain and normalized to ε_{full}^T.

The nonuniform guide magnetic field present in this reconnection event affects its geometry. Despite the 3D nature of this event, for the diffusion region in which $|\boldsymbol{B}| \leqslant 0.4 B_0$, we observe gyrotropic/agyrotropic patterns (Section 3.3) similar to those observed in 2D laminar reconnection without a guide field (Yin et al. 2001). However, given the complex geometry of our event, we do not observe gyrotropic/agyrotropic patterns matching 2D reconnection in the part of the diffusion region below the x-points. Moreover, we do not observe a quadrupolar pattern of the in-plane component $\Pi_{pr,e}$ (Figure 4(d)) within the diffusion region, which is characteristic of agyrotropy in 2D reconnection without a guide field (Yin et al. 2001).

In the reconnection event that we analyze, although of turbulent nature, the out-of-plane electron motion is consistent with the 3D shape of electron diffusion regions observed in laboratory plasmas (Furno et al. 2005; Yoo et al. 2013; Yamada et al. 2014).

In our event, $d\varepsilon_e^k/dt > 0$ along the separatrices and $d\varepsilon_e^k/dt < 0$ in the outer part of the reconnecting magnetic island (Figure 6(a)). This corresponds to the acceleration of electrons along the separatrices (Figure 6(c)) and the presence of a stagnation region. The shear between the flux ropes increases the electron thermal energy and pressure, and the bulk kinetic energy reduces at the stagnation point.

At the locations of the separatrices, $\boldsymbol{u}_e \cdot \nabla \cdot \overline{\boldsymbol{P}}_e > 0$ (Figure 6(b)). This suggests electron streams that increase the electron pressure. Conversely, $\boldsymbol{u}_e \cdot \nabla \cdot \overline{\boldsymbol{P}}_e < 0$ in the region between the x-points. This suggests electron streams that reduce the electron pressure and push the plasma within the diffusion region to a local thermal equilibrium. While reconnection is occurring, the high-pressure electrons fill the diffusion region.

Within the diffusion region, the electric field increases the electron kinetic energy density, and the work done by the electric field on the electrons $-q_e n_e(\boldsymbol{u}_e \cdot \boldsymbol{E})$ partially balances with the advection of the electron pressure. This is consistent with previous studies (Fadanelli et al. 2021).

The irreversible electron energy density change Ξ_e^k (Figure 6(e)) is nonzero everywhere in the vicinity of the reconnecting structures. The quantity Ξ_e^k displays structures with positive and negative values within the magnetic islands, suggesting that collisional processes accelerate and decelerate electron bulk flows within the magnetic islands. Conversely, in the diffusion region, the positive value of Ξ_e^k indicates that electrons are irreversibly accelerated.

Unlike previous studies of turbulent reconnection (Fadanelli et al. 2021), we estimate the electron thermal energy transfer associated with each term of Equation (11). Compared to the case of the kinetic power density, the thermal power density terms present stronger fluctuations. This is evident when
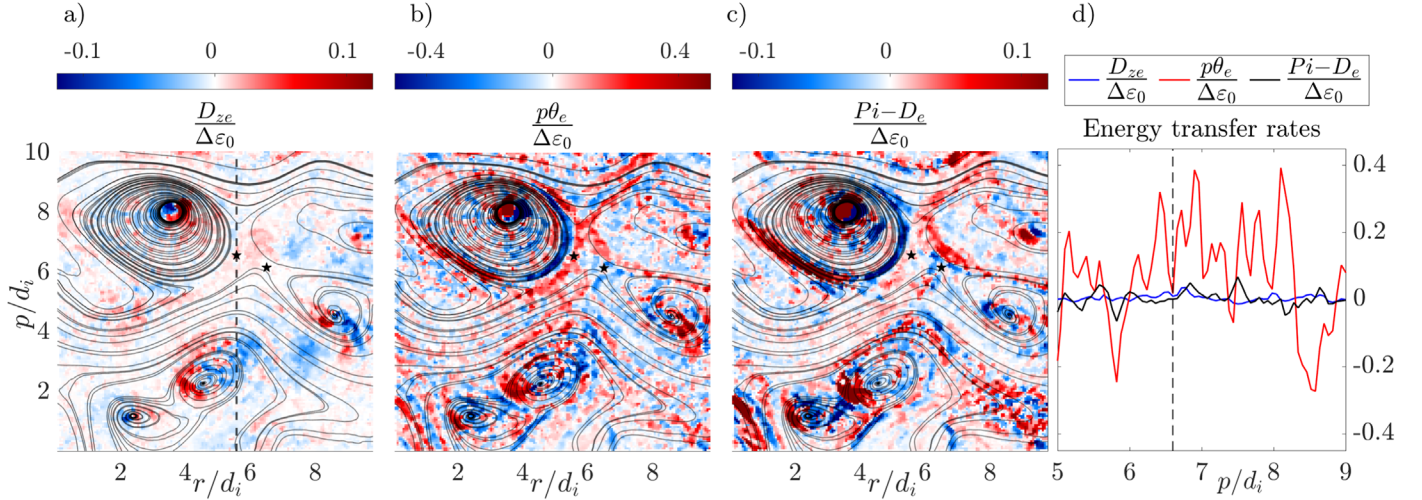
Figure 11. Damping and heating proxies at the simulation time $t = 120\omega_{pi}^{-1}$. (a) 2D cuts in the r-p plane of the Zenitani parameter for electrons D_{ze}. (b) Diagonal part of the strain pressure interaction $p\theta_e$. (c) Off-diagonal part of the strain pressure interaction $Pi - D_e$. (d) 1D cut of these terms as in Figure 7.

comparing $d\varepsilon_e^k/dt$ (Figure 6(a)) and $d\varepsilon_e^{th}/dt$ (Figure 6(f)), as well as comparing $\varepsilon_e^k \nabla \cdot \boldsymbol{u}_e$ (Figure 6(c)) and $\varepsilon_e^{th} \nabla \cdot \boldsymbol{u}_e$ (Figure 6(i)). This difference suggests that the electron bulk flows more efficiently transport thermal energy density than bulk kinetic energy density.

The power density terms associated with the compression/expansion of the flow $\nabla \boldsymbol{u}_e : \overline{\boldsymbol{P}}_s$ and $\varepsilon_e^{th} \nabla \cdot \boldsymbol{u}_e$ exhibit a strong coherence with the electron motion along the reconnection separatrices. The electron streams gain thermal energy (i.e., heating) associated with the reconnection. This is consistent with simulations of fast collisionless reconnection at low β (Loureiro et al. 2013) and observations of magnetospheric reconnection (Chasapis et al. 2017; Holmes et al. 2019).

The most important contribution to $\nabla \boldsymbol{u}_e : \overline{\boldsymbol{P}}_s$ comes from the isotropic part of the strain pressure term. Correspondingly, $\varepsilon_e^{th} \nabla \cdot \boldsymbol{u}_e$ presents patterns similar to $\nabla \boldsymbol{u}_e : \overline{\boldsymbol{P}}_s$. Moreover, the contribution of the off-diagonal elements in $\nabla \boldsymbol{u}_e$ and $\overline{\boldsymbol{P}}_e$ to the thermal energy transport is less than the isotropic contribution, which is consistent with previous studies of turbulent reconnection (Bandyopadhyay et al. 2021; Fadanelli et al. 2021). The terms associated with electron compressibility ($\varepsilon_e^{th} \nabla \cdot \boldsymbol{u}_e$ and $\nabla \boldsymbol{u}_e : \overline{\boldsymbol{P}}_s$) are typically greater than the heat flux contribution ($\nabla \cdot \boldsymbol{h}_s$), suggesting that, for collisionless reconnection, compressible thermal energy density transport is important for electrons. On average, within the subdomain, the electrons gain kinetic energy at the expense of the electric field (Figure 8(d)). The electrons both lose and gain thermal energy (Figures 8(g) and (h)) predominantly along thin sheet-like structures.

Similar to the irreversible kinetic energy density transfer Ξ_e^k, the irreversible thermal energy transfer Ξ_e^{th} is nonzero within the reconnecting structures, as well as within the diffusion region. Moreover, electrons irreversibly gain thermal energy density at the location of the separatrices and within the diffusion region.

The irreversible kinetic energy density transfer is mainly confined to the flux ropes in our simulation (Figure 9(a)). Conversely, the irreversible thermal energy density transfer (Figure 9(b)) occurs in thin sheet-like structures that extend for over $5d_i$.

Although $\langle \Xi_e^k \rangle$ is negligible compared to $\Delta \varepsilon_e^k$ (Figure 10(b)), the fact that Ξ_e^k is comparable in magnitude to $q_e n_e \boldsymbol{E} \cdot \boldsymbol{u}_e$ and $\boldsymbol{u}_e \cdot \nabla \cdot \overline{\boldsymbol{P}}_e$ (Figure 7(a)) implies that Ξ_e^k must be considered in the local kinetic energy transfer of electrons, as it includes important information about the oscillating energy associated with instantaneous field–particle correlations (Klein & Howes 2016; Howes et al. 2017; Klein et al. 2017). Only meaningful averages of the nonlinear correlations between the fluctuating electric field and the fluctuating perturbation of the distribution function define the secular transfer of energy from the fields to the particles. Therefore, we propose that an energy balance analysis based on the energy density expressions derived from the collisionless Vlasov equation is not entirely accurate for kinetic simulations. Because numerical effects in kinetic simulations act as an effective collision operator, the energy balance equations derived from the Vlasov equation without provision for the terms on the right-hand side of Equation (1) are not exactly satisfied.

Comparing our results with damping (D_{ze}) and heating ($p\theta_e$ and $Pi - D_e$) proxies (Pezzi et al. 2021), we observe that fluctuations of $p\theta_e$ inside the diffusion region (Figure 11(d)) are typically greater than fluctuations of D_{ze} and $Pi - D_e$. Integrating over the subdomain (not shown here), we find that $p\theta_e/\Delta\varepsilon_0|_V > |Pi-D_e|/\Delta\varepsilon_0|_V$. This suggests that, within the subdomain, the electron heating is mostly due to compressive effects. This is consistent with results from turbulent simulations (Pezzi et al. 2021) and observations of turbulent reconnection (Bandyopadhyay et al. 2021) but not with results from simulations of laminar reconnection.

The proxies $p\theta_e$ and $Pi - D_e$ share the same signs at most locations in our simulation domain. However, in the diffusion region near the null region, the opposite sign of $Pi - D_e$ and $p\theta_e$ suggests that agyrotropic heating mechanisms can emerge to compensate for any reduction or increase in the thermal energy density due to isotropic heating mechanisms. Moreover, integrating over the subdomain and over time, we find that $p\theta_e|_{V,t} = 0.0137$ and $Pi - D_e|_{V,t} = -0.0190$ in the units used in Figure 11. This suggests that $p\theta_e$ is greater than $Pi - D_e$ within the diffusion region at the particular time selected but not throughout the whole simulation, due to a local effect.

The positive values of D_{ze} and the negative value of $p\theta_e$ and $Pi - D_e$ in the region between the x-points suggest that electrons gain kinetic energy density from the fields while losing thermal energy density. Between the x-points, the electric field accelerates electrons (Figure 6(d)). The increase in the electrons' kinetic energy density may be due to Landau damping (Landau 1946; Howes et al. 2006; Li et al. 2016). Conversely, the magnetic pressure (not shown here) increases near the region between the x-points. The total pressure balance requires a depletion of p_e and p_i (as confirmed by Figures 3(a) and (e)) in the diffusion region. Plasma pressure depletion has been suggested to be responsible for the onset of fast reconnection in collisionless plasmas (Liu et al. 2022). Thus, the expansion and the consequential cooling off of the electrons reduce their thermal energy.

5. Conclusions

We derive a framework to quantify the collision-like effects that lead to irreversible energy transfer and thus dissipation in PIC plasmas. We identify and locate magnetic reconnection as a key mechanism for heating, damping, and dissipation in plasma turbulence in low-collisionality systems like the solar wind.

Previously, the transfer and transport of energy in plasmas with low collisionality have been studied separately in simulations of reconnection (Hesse & Winske 1998; Hesse et al. 2001; Zenitani et al. 2011; Muñoz et al. 2017; Pucci et al. 2018; Pezzi et al. 2019, 2021) and turbulence (Wan et al. 2012; Yang et al. 2017; Li et al. 2019; Pezzi et al. 2021). The transfer and transport in magnetic reconnection that forms from a turbulent cascade have been limited to 2D geometries (Parashar et al. 2009; Fadanelli et al. 2021) and observations (Chasapis et al. 2018; Bandyopadhyay et al. 2020), while the 3D case has received little attention. We study, for the first time, the energy transport associated with 3D magnetic reconnection that occurs as a consequence of a turbulent cascade to a high level of detail and including all power density terms resulting from the full Boltzmann equation. We extend the analysis of similar studies (Fadanelli et al. 2021) by exploring the transfer and transport of thermal energy for electrons.

The energy transfer and transport in collisionless plasmas is believed to be governed by nonthermal and kinetic mechanisms such as resonant (Marsch et al. 2003; Kasper et al. 2008) and nonresonant heating processes (Chandran et al. 2010, 2013). However, the irreversible energy transport is ultimately associated with collisional effects (Schekochihin et al. 2009).

The agyrotropy signatures present in the reconnection diffusion region and in the reconnecting magnetic structures allow for agyrotropic energy transfer mechanisms such as agyrotropy-driven instabilities to take place not only near the electron diffusion region (Ricci et al. 2004; Roytershteyn et al. 2012; Graham et al. 2017) but also within the reconnecting magnetic structures. These signatures are 3D, as they extend in the a-direction for over $5d_i$. A future study of the instabilities that occur during a 3D turbulent reconnection event would be worthwhile to enhance our understanding of the collisionless energy dissipation.

We show that the contributions to the energy density transfer from the effective collision terms are not negligible. To determine the exact source of these contributions, future work must use a large number of particles while keeping the 3D geometry. In addition, the inclusion of a controllable collision operator would allow for a detailed study of collisions in 3D reconnection (Pezzi 2017; Donnel et al. 2019; Boesl et al. 2020; Pezzi et al. 2021).

The general framework that we introduce is suitable for estimating the irreversible energy density transfer in the solar wind. For instance, Equations (8) and (11) can be applied to spacecraft data to study the radial evolution of energy as a function of heliospheric distance in the solar wind. This work would be of interest for the energetics of both solar wind electrons (Scime et al. 1994; Innocenti et al. 2020) and solar wind protons (Matteini et al. 2007; Hellinger et al. 2011; Adhikari et al. 2020).

Appendix
Derivation of the Equations for the Energy Densities

To derive the nth moment of the Boltzmann Equation (1), we take the dyadic product of Equation (1) with $\boldsymbol{v}^n$ on the left and integrate the equation over the entire velocity space. The zeroth moment leads to

$$\frac{\partial n_s}{\partial t} + \nabla \cdot (n_s \boldsymbol{u}_s) = \Xi_s^0. \tag{A1}$$

The collision operator has the property $\Xi_s^0 = 0$, as it must conserve the number of particles. In this case, Equation (A1) is the continuity equation. The first moment leads to

$$\frac{\partial (n_s \boldsymbol{u}_s)}{\partial t} + \frac{1}{m_s}\nabla \cdot \overline{\mathbb{P}}_s - \frac{q_s}{m_s}n_s(\boldsymbol{E} + \boldsymbol{u}_s \times \boldsymbol{B}) = \boldsymbol{\Xi}_s^1, \tag{A2}$$

where

$$\overline{\mathbb{P}}_s \equiv m_s \int f_s \boldsymbol{v}\boldsymbol{v} d^3v. \tag{A3}$$

We separate the second moment in Equation (A3) according to $\nabla \cdot \overline{\mathbb{P}} = \nabla \cdot \overline{\boldsymbol{P}} + \nabla \cdot (nm\boldsymbol{u}\boldsymbol{u})$, where $\overline{\boldsymbol{P}}$ is defined in Equation (4). Invoking Equation (A1), Equation (A2) takes the form

$$\frac{d(n_s m_s \boldsymbol{u}_s)}{dt} = -\nabla \cdot \overline{\boldsymbol{P}}_s - (\nabla \cdot \boldsymbol{u}_s)n_s m_s \boldsymbol{u}_s$$
$$+ q_s n_s(\boldsymbol{E} + \boldsymbol{u}_s \times \boldsymbol{B}) + m_s \boldsymbol{\Xi}_s^1. \tag{A4}$$

This equation describes the total change in time of the bulk momentum density for each species.

The second moment of Equation (1) yields

$$
\begin{aligned}
&\frac{\partial \overline{\overline{P}}_s}{\partial t} + \nabla \cdot [(Q_{ijk,s} + u_{i,s}P_{ij,s} + P_{ij,s}u_{k,s} + u_{j,s}P_{ik,s})) \\
&\times \hat{e}^i \otimes \hat{e}^j \otimes \hat{e}^k] \\
&- \frac{q_s}{m_s}(\overline{\overline{P}}_s \times \boldsymbol{B} - \boldsymbol{B} \times \overline{\overline{P}}_s) = -\nabla \cdot (n_s m_s \boldsymbol{u}_s \boldsymbol{u}_s \boldsymbol{u}_s) \\
&- \frac{\partial(n_s m_s \boldsymbol{u}_s \boldsymbol{u}_s)}{\partial t} \\
&+ q_s n_s \left[\boldsymbol{E}\boldsymbol{u}_s + \boldsymbol{u}_s \boldsymbol{E} + \frac{1}{m_s}((\boldsymbol{u}_s \boldsymbol{u}_s) \times \boldsymbol{B} - \boldsymbol{B} \times (\boldsymbol{u}_s \boldsymbol{u}_s)) \right] \\
&+ m_s \overline{\overline{\Xi}}_s^2,
\end{aligned}
\tag{A5}
$$

where $Q_{ijk,s}$ represent the elements of the heat flux tensor

$$
\overline{\overline{\overline{Q}}}_s \equiv m_s \int f_s (\boldsymbol{v} - \boldsymbol{u}_s)(\boldsymbol{v} - \boldsymbol{u}_s)(\boldsymbol{v} - \boldsymbol{u}_s) d^3 v.
\tag{A6}
$$

Equations (A4) and (A5) are the exact first and second moments of Equation (1).

We proceed to derive expressions for the energy densities ε_s^k and $\varepsilon_s^{\text{th}}$. For this purpose, we take the scalar product of Equation (A4) with $\boldsymbol{u}_s$, which leads to Equation (8). To obtain an expression for the thermal energy ε^{th}, we take the trace of Equation (A5). For the calculation of the trace of the cross product terms in Equation (A5), we use an element-wise approach. If $\boldsymbol{A}$ is a vector and $\overline{\overline{M}}$ is a tensor of rank two, the cross product is defined as $\boldsymbol{A} \times \overline{\overline{M}} = \epsilon_{lip} A_i M_{pq} \hat{e}^l \otimes \hat{e}^q$. It can be shown that $\overline{\overline{M}} \times \boldsymbol{A} = -(\boldsymbol{A} \times \overline{\overline{M}}^T)^T$, where $\overline{\overline{M}}^T$ is the transpose of $\overline{\overline{M}}$ and $\text{Tr}(\boldsymbol{A} \times \overline{\overline{M}}) = \epsilon_{ijk} A_i M_{jk}$. Moreover, if $\overline{\overline{M}}$ is a symmetric tensor, then $\text{Tr}(\boldsymbol{A} \times \overline{\overline{M}}) = 0$. In addition, the trace of $\nabla \cdot \overline{\overline{\overline{Q}}}$ corresponds to $2\nabla \cdot \boldsymbol{h}$. This procedure leads to

$$
\begin{aligned}
&\frac{d\varepsilon_s^{\text{th}}}{dt} + \frac{d\varepsilon_s^k}{dt} + \nabla \cdot \boldsymbol{h}_s + \nabla \boldsymbol{u}_s : \overline{\overline{P}}_s + (\nabla \cdot \boldsymbol{u}_s)\varepsilon_s^{\text{th}} \\
&+ \boldsymbol{u}_s \cdot (\nabla \cdot \overline{\overline{P}}_s) = -(\nabla \cdot \boldsymbol{u}_s)\varepsilon_s^k + q_s n_s \boldsymbol{E} \cdot \boldsymbol{u}_s \\
&+ \frac{1}{2} Tr(m_s \overline{\overline{\Xi}}_s^2).
\end{aligned}
\tag{A7}
$$

Combining Equations (8) and (A7), we obtain Equation (11).

ORCID iDs

Jeffersson A. Agudelo Rueda ⬤ https://orcid.org/0000-0001-5045-0323
Daniel Verscharen ⬤ https://orcid.org/0000-0002-0497-1096
Robert T. Wicks ⬤ https://orcid.org/0000-0002-0622-5302
Christopher J. Owen ⬤ https://orcid.org/0000-0002-5982-4667
Georgios Nicolaou ⬤ https://orcid.org/0000-0003-3623-4928
Kai Germaschewski ⬤ https://orcid.org/0000-0002-8495-6354
Andrew P. Walsh ⬤ https://orcid.org/0000-0002-1682-1212
Ioannis Zouganelis ⬤ https://orcid.org/0000-0003-2672-9249
Santiago Vargas Domínguez ⬤ https://orcid.org/0000-0002-5999-4842

References

Adhikari, L., Zank, G. P., Zhao, L.-L., et al. 2020, ApJS, 246, 38
Adhikari, S., Parashar, T. N., Shay, M. A., et al. 2021, PhRvE, 104, 065206
Agudelo Rueda, J. A., Verscharen, D., Wicks, R. T., et al. 2021, JPlPh, 87, 905870228

Bandyopadhyay, R., Chasapis, A., Matthaeus, W. H., et al. 2021, PhPl, 28, 112305
Bandyopadhyay, R., Matthaeus, W. H., Parashar, T. N., et al. 2020, PhRvL, 124, 255101
Barnes, A. 1968, ApJ, 154, 751
Birdsall, C. K., & Langdon, A. B. 2018, Plasma Physics via Computer Simulation (Boca Raton, FL: CRC Press), doi:10.1201/9781315275048
Boesl, M., Bergmann, A., Bottino, A., et al. 2020, CoPP, 60, e201900117
Chandran, B., Verscharen, D., Quataert, E., et al. 2013, ApJ, 776, 45
Chandran, B. D., Li, B., Rogers, B. N., Quataert, E., & Germaschewski, K. 2010, ApJ, 720, 503
Chasapis, A., Matthaeus, W., Parashar, T., et al. 2017, ApJ, 836, 247
Chasapis, A., Yang, Y., Matthaeus, W., et al. 2018, ApJ, 862, 32
Coleman, P. J., Jr 1968, ApJ, 153, 371
Dawson, J. M. 1983, RvMP, 55, 403
Donnel, P., Garbet, X., Sarazin, Y., et al. 2019, CoPhC, 234, 1
Fadanelli, S., Lavraud, B., Califano, F., et al. 2021, JGRA, 126, e2020JA028333
Feldman, W., Asbridge, J., Bame, S., Gosling, J., & Lemons, D. 1978, JGRA, 83, 5285
Feldman, W., Asbridge, J., Bame, S., Montgomery, M., & Gary, S. 1975, JGR, 80, 4181
Franci, L., Cerri, S. S., Califano, F., et al. 2017, ApJL, 850, L16
Furno, I., Intrator, T. P., Hemsing, E. W., et al. 2005, PhPl, 12, 055702
Gary, S. P. 1999, JGRA, 104, 6759
Gazis, P. R., & Lazarus, A. J. 1982, GeoRL, 9, 431
Germaschewski, K., Fox, W., Abbott, S., et al. 2016, JCoPh, 318, 305
Goldstein, M., Wicks, R., Perri, S., & Sahraoui, F. 2015, RSPTA, 373, 20140147
Graham, D. B., Khotyaintsev, Y. V., Vaivads, A., et al. 2017, PhRvL, 119, 025101
Greco, A., Valentini, F., Servidio, S., & Matthaeus, W. 2012, PhRvE, 86, 066405
Grošelj, D. 2019, PhD thesis, LMU Munich
Hammett, G. W., & Perkins, F. W. 1990, PhRvL, 64, 3019
Hellinger, P., Matteini, L., Štverák, Š., Trávníček, P. M., & Marsch, E. 2011, JGRA, 116, A09105
Hesse, M., Birn, J., & Kuznetsova, M. 2001, JGRA, 106, 3721
Hesse, M., & Schindler, K. 1988, JGRA, 93, 5559
Hesse, M., & Winske, D. 1998, JGRA, 103, 26479
Hockney, R. 1971, JCoPh, 8, 19
Holmes, J., Ergun, R., Nakamura, R., et al. 2019, JGRA, 124, 8788
Howes, G. G., Cowley, S. C., Dorland, W., et al. 2006, ApJ, 651, 590
Howes, G. G., Klein, K. G., & Li, T. C. 2017, JPlPh, 83, 705830102
Innocenti, M. E., Boella, E., Tenerani, A., & Velli, M. 2020, ApJL, 898, L41
Kasper, J., Lazarus, A., & Gary, S. 2008, PhRvL, 101, 261103
Kaufmann, R. L., & Paterson, W. R. 2009, JGRA, 114, A00D04
Kiyani, K. H., Osman, K. T., & Chapman, S. C. 2015, RSPTA, 373, 20140155
Klein, K. G., & Howes, G. G. 2016, ApJL, 826, L30
Klein, K. G., Howes, G. G., & TenBarge, J. M. 2017, JPlPh, 83, 535830401
Klimontovich, Y. L. 1997, PhyU, 40, 21
Klimontovich, Y. L. 2013, The Statistical Theory of Non-equilibrium Processes in a Plasma: International Series of Monographs in Natural Philosophy, Vol. 9 (Amsterdam: Elsevier), doi:10.1016/C2013-0-06978-2
Kowal, G., Falceta-Gonçalves, D. A., Lazarian, A., & Vishniac, E. T. 2017, ApJ, 838, 91
Landau, L. D. 1946, Oscillations of an Electron Plasma (Moscow: Academy of Sciences USSR, Institute for Physical Problems)
Lapenta, G., Pucci, F., Goldman, M., & Newman, D. 2020, ApJ, 888, 104
Lazarian, A., Eyink, G. L., Jafari, A., et al. 2020, PhPl, 27, 012305
Li, T. C., Howes, G. G., Klein, K. G., Liu, Y.-H., & TenBarge, J. M. 2019, JPlPh, 85, 905850406
Li, T. C., Howes, G. G., Klein, K. G., & TenBarge, J. M. 2016, ApJL, 832, L24
Liang, H., Cassak, P. A., Servidio, S., et al. 2019, PhPl, 26, 082903
Liu, Y.-H., Cassak, P., Li, X., et al. 2022, CmPhy, 5, 97
Loureiro, N., Schekochihin, A., & Zocco, A. 2013, PhRvL, 111, 025002
Loureiro, N. F., & Boldyrev, S. 2017, PhRvL, 118, 245101
Loureiro, N. F., & Boldyrev, S. 2020, ApJ, 890, 55
Marsch, E., Mühlhäuser, K.-H., Schwenn, R., et al. 1982, JGRA, 87, 52
Marsch, E., & Tu, C.-Y. 1990, JGRA, 95, 11945
Marsch, E., Vocks, C., & Tu, C.-Y. 2003, NPGeo, 10, 101
Matteini, L., Landi, S., Hellinger, P., et al. 2007, GeoRL, 34, L20105
Matthaeus, W. H., Yang, Y., Wan, M., et al. 2020, ApJ, 891, 101
Matthaeus, W. H., Zank, G. P., Smith, C. W., & Oughton, S. 1999, PhRvL, 82, 3444

McComas, D., Bame, S., Feldman, W., Gosling, J., & Phillips, J. 1992, GeoRL, 19, 1291

Muñoz, P., Büchner, J., & Kilian, P. 2017, PhPl, 24, 022104

Ng, J., Hakim, A., Bhattacharjee, A., Stanier, A., & Daughton, W. 2017, PhPl, 24, 082112

Ng, J., Huang, Y.-M., Hakim, A., et al. 2015, PhPl, 22, 112104

Parashar, T., Shay, M., Cassak, P., & Matthaeus, W. 2009, PhPl, 16, 032310

Pezzi, O. 2017, JPlPh, 83, 555830301

Pezzi, O., Liang, H., Juno, J., et al. 2021, MNRAS, 505, 4857

Pezzi, O., Yang, Y., Valentini, F., et al. 2019, PhPl, 26, 072301

Pontin, D. 2011, AdSpR, 47, 1508

Pucci, F., Servidio, S., Sorriso-Valvo, L., et al. 2017, ApJ, 841, 60

Pucci, F., Usami, S., Ji, H., et al. 2018, PhPl, 25, 122111

Ricci, P., Brackbill, J., Daughton, W., & Lapenta, G. 2004, PhPl, 11, 4489

Roytershteyn, V., Daughton, W., Karimabadi, H., & Mozer, F. 2012, PhRvL, 108, 185001

Schekochihin, A., Cowley, S., Dorland, W., et al. 2009, ApJS, 182, 310

Schindler, K., Hesse, M., & Birn, J. 1988, JGRA, 93, 5547

Schmitz, H., & Grauer, R. 2006, PhPl, 13, 092309

Scime, E. E., Bame, S. J., Feldman, W. C., et al. 1994, JGRA, 99, 23401

Scudder, J., & Daughton, W. 2008, JGRA, 113, A10208

Servidio, S., Matthaeus, W., Shay, M., et al. 2010, PhPl, 17, 032315

Sundkvist, D., Retinò, A., Vaivads, A., & Bale, S. D. 2007, PhRvL, 99, 025004

Wan, M., Matthaeus, W., Karimabadi, H., et al. 2012, PhRvL, 109, 195001

Wang, L., Germaschewski, K., Hakim, A., et al. 2018, JGRA, 123, 2815

Wang, L., Hakim, A. H., Bhattacharjee, A., & Germaschewski, K. 2015, PhPl, 22, 012108

Yamada, M., Yoo, J., Jara-Almonte, J., et al. 2014, NatCo, 5, 4774

Yang, Y., Matthaeus, W. H., Parashar, T. N., et al. 2017, PhPl, 24, 072306

Yin, L., Winske, D., Gary, S., & Birn, J. 2001, JGRA, 106, 10761

Yoo, J., Yamada, M., Ji, H., & Myers, C. E. 2013, PhRvL, 110, 215007

Zenitani, S., Hesse, M., Klimas, A., & Kuznetsova, M. 2011, PhRvL, 106, 195003

Zweibel, E. G., & Yamada, M. 2016, RSPSA, 472, 20160479